Master thesis. Universitat Politècnica de Catalunya (UPC)

IFAE-UAB Raman LIDAR Link Budget and Components

Miguel Eizmendi

Thesis advisors
Dr. Michele Doro (UAB)
Dr. Francesc Rocadenbosch (UPC)

Barcelona, September 2011

AKNOWLEDGEMENTS

Este documento es fruto del esfuerzo de varias personas e instituciones que participaron directa o indirectamente en él; leyendo, revisando, opinando y dándome ánimos.

Especialmente quería agradecer su colaboración a:

El equipo de IFAE-UAB que escucharon mis dudas y propuestas en cada reunión semanal. En particular quiero agradecer a Michele Doro, co-director de esta tesis, su paciencia y apoyo que me ha mostrado durante estos meses.

Francesc Rocadenbosch, co-director de esta tesis, y Dhiraj Kumar por su ayuda y contribución a este trabajo, así como también la oportunidad de participar en el artículo que aparece en el anexo de este documento.

Xènia y Matias, compañeros de piso y amigos, por apoyarme en estos meses difíciles y por ayudarme con la revisión de este documento. En general, también a todos mis amigos y familia que me han dado apoyo y ánimos imprescindibles.

Gracias a todos.

ABSTRACT

Ground-based Cherenkov telescopes of the Imaging Atmospheric Cherenkov Telescope (IACT) class observe cosmic gamma-rays by collecting the Cherenkov light formed in atmospheric electromagnetic showers initiated by primary gamma-ray impinging onto the top Earth atmosphere. The reconstructed energy of the cosmic gamma-ray is affected by the electromagnetic shower development in the atmosphere. Different atmospheric conditions (haze, cloud, etc) can affect the energy reconstruction and thus the overall performance of the telescope.

LIDAR (light detection and ranging) are devices that are able to measure various atmospheric parameters in range of altitudes. They are constituted by a laser emitting toward the atmosphere, a telescope collecting the backscattered LIDAR light, an optical system to separate and focus different return wavelengths and a read-out system. Two instituted in Barcelona: the Insitut de Física d'Altes Energies (IFAE) and the Universitat Autònoma de Barcelona (UAB) are developing a LIDAR optimized for usage for IACTs to monitor and measure the atmosphere at the telescope site and reduce the uncertainties in the energy reconstruction.

In this thesis, a full link-budget analysis of this LIDAR is presented, discussing the effects that different choices for the LIDAR subsystems (photomultipliers, filters bandwidth, etc) have on the LIDAR response in terms of maximum range, integration time, and signal-to-noise ratio. This study allowed to finalize the LIDAR design layout and characterize its performance. In addition, a full simulation based on the software ZEMAX^{TM} of the polychromator system is presented. In this part, a collimating system has been design to allow for a 2- or 3-channels read-out configuration. Commercial solutions for lenses, mirror and filters are also discussed. As a result of this part, we show that a simple collimating system is working for up to 3 channels while additional read-out channels would require a more sophisticate design.

INDEX

Chapter 1. Introduction

The history of astronomy is as old as the history of human-being. Almost all ancient religions tried to explain the origin of the universe through mythology. Throughout recorded history, several theories like geocentric, heliocentric and the Newtonian model of the Solar System arose from the observation of the universe. All these theories have tried to explain how the universe works and it is clear proof of the human commitment on knowing more about the unknown.
Initially, universe studies were limited to the observation and prediction of the motion of objects visible to the naked eye. Galileo, who improved the Copernicus' heliocentric theory, revolutionized the astronomy field by using a telescope in his observations. From then, new models arrived in which the Solar System is located in the Milky Way, a galaxy composed of billions of stars. The introduction of spectrometry enabled scientists to understand that the stars where similar to the sun differing only in size, mass and temperature. All this new information has given form to what we know as the modern astronomy.
Nowadays we do not longer conceive the sky observation as just looking through a telescope but we now see it as deciphering the universe emission over the whole electromagnetic spectrum. In the last century, the radio astronomy has provided compelling evidence for the Big Bang theory and has allowed the discovery of new elements like quasars, pulsars, blazars, black holes and neutron stars. Nowadays, research is still very active.

1.1. Gamma-ray astronomy. MAGIC and CTA

We could say that radio astronomy was born by accident in the 30s. With the advent of the first radio receivers, some repeating signals of unknown origin were detected firstly as noise. After a few years, it was proven that this signal was cosmic radiation. During World War II, advances in the development of RADAR techniques boosted radio astronomy. This was possible because the atmosphere is transparent at radio frequencies, whereas other frequencies are blocked and cannot pass through it. The observational astronomy is divided according to the observed region of the electromagnetic spectrum in Infrared, Optical, Ultraviolet, X-ray and Gamma-ray Astronomy. Their associated atmosphere opacity is shown in Figure 1.

The atmosphere protects the earth from gamma radiation. First experiments for gamma rays detection used balloons first and satellites after. Gamma astronomy is also known as the astronomy of the 'violent' universe because the events that produce these rays are catastrophic events like supernova explosions, high speed collisions or black holes. These high energy gamma-rays, when reaching the Earth and interacting with the atmosphere, eventually produce Cherenkov radiation (see Cherenkov radiation explanation below) detectable from ground-based telescopes.

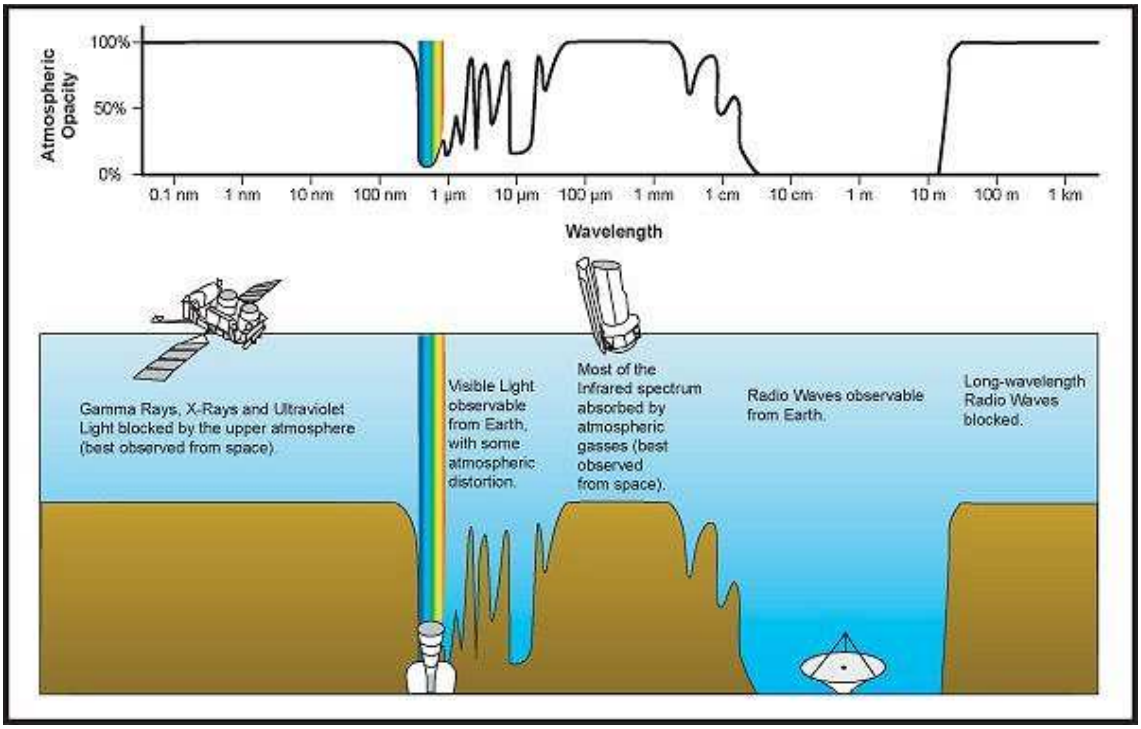

Figure 1. Relationship between atmospheric opacity and wavelength of light (NASA/IPAC)

MAGIC (Major Atmospheric Gamma-ray Imaging Cherenkov Telescope) is an international scientific collaboration of research institutes and universities from Spain, Germany, Italy, Finland, Poland, Switzerland, Croatia and Bulgaria. The main scope of MAGIC is the indirect detection of gamma rays of very high energy (50 GeV – 10 TeV) through the observation of the Cherenkov radiation that they produce. The detection of these high energy rays is much more complicated by means of satellite-telescopes because it requires very large detection areas.

Figure 2. Picture of MAGIC telescope in La Palma.

The project started in the early 90s but the first telescope did not start operating until 2004. It was the telescope placed in the Roque de los Muchachos observatory in the island of La Palma (Spain) at 2200 meters above sea level.

The location was chosen because of its good weather conditions all year round, in terms of atmospheric transparency. The main characteristics of the telescope are a 17 meters diameter for the reflecting surface (so far it was the largest in the world), a camera build with 577 high sensitive photomultipliers with a field of view of 3.5º. A second MAGIC telescope of essentially the same characteristics (MAGIC-II) started taking data in July 2009. With the stereoscopic system the sensitivity of the observatory increases about 3 times.

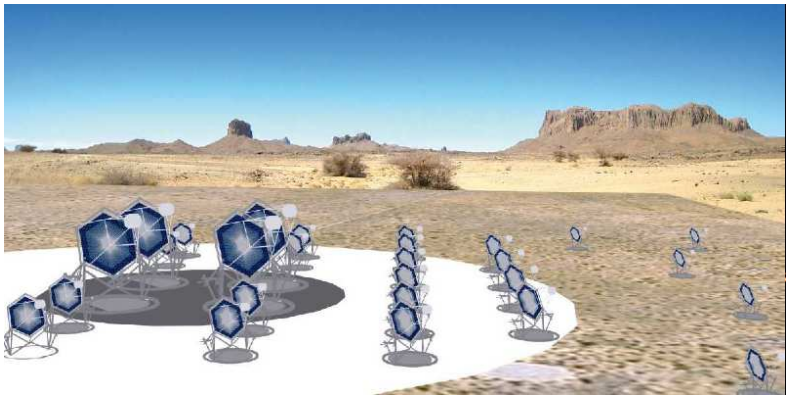

Figure 3. Artistic view of the compound different size telescopes CTA system. The area coverage is of 1–10 km2.

Nowadays most of the collaborators of MAGIC are working on the Cherekov Telescope Array (CTA) project. The goal of the CTA project is constructing a matrix of tens of Cherenkov telescopes with sensitivity 10 times higher than in MAGIC. Actually, CTA involves two telescope arrays: the first one in the northern hemisphere for the study of extragalactic objects at low energies and the second one at the southern hemisphere which will consist of three types of telescopes with different mirror sizes in order to cover the full energy range (10 GeV – 100 TeV). The design foresees a factor of 5-10 improvement in sensitivity in the current very high energy gamma ray domain of about 100 GeV to some 10 TeV, and an extension of the accessible energy range from well below 100 GeV to above 100 TeV.

1.2. Cherenkov radiation

The speed of light depends on the medium it is traveling through. In vacuum the speed of light is a fundamental physical constant and cannot be exceeded. But when light travels through a different medium the speed is reduced by a factor n which corresponds to the refractive index of the material, so that in a medium $V_{light} = c/n$. If a charged particle passes through a dielectric medium, like the atmosphere, at a speed greater than the speed of light in such medium it might emit Cherenkov radiation. The charged particle asymmetrically polarizes Nitrogen and Oxygen (the main components in the atmosphere) molecules around its trajectory. The polarization is asymmetrical since the molecules ahead the particles have not been yet polarized whereas the ones behind the particle are polarized. Ahead molecules have not been polarized because the particle travels faster than its own electric field.

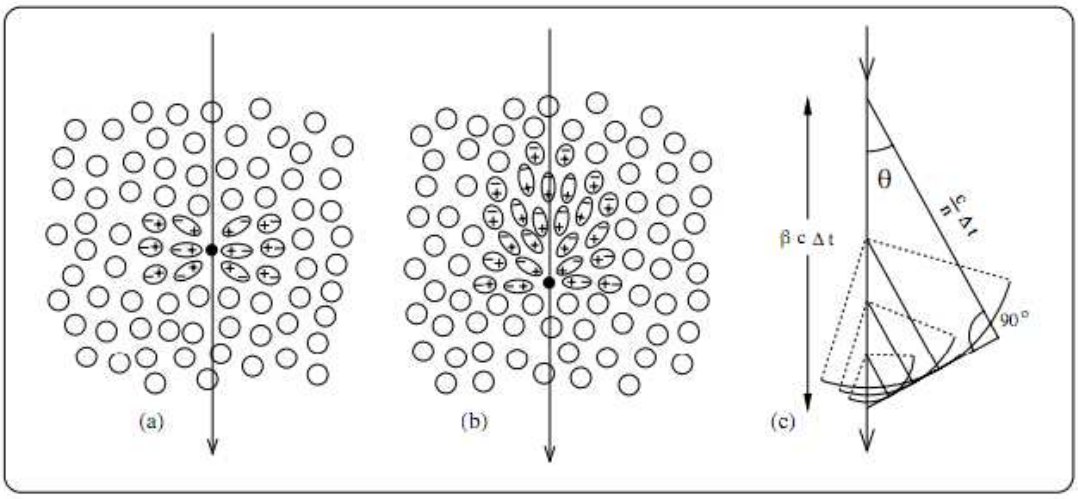

Figure 4. Polarization produced in a dielectric medium by a charged particle. (a) Small velocity. (b) High velocity. (c) Construction of the Cherenkov light wavefront. [1]

When the atmosphere molecules return to the original situation of equilibrium they emit photons. In normal circumstances no radiation is emitted Figure 4 (a) but given that the particle travels faster than the emitted photons (b), the wavefronts emitted in different points of the particle's trajectory can sum coherently (c). Constructive interferences of spherical wavefronts end with a unique wavefront and the result is a shock wave created behind the traveling particle. This phenomenon is similar to the generation of a shock wave when the speed of sound is exceeded.

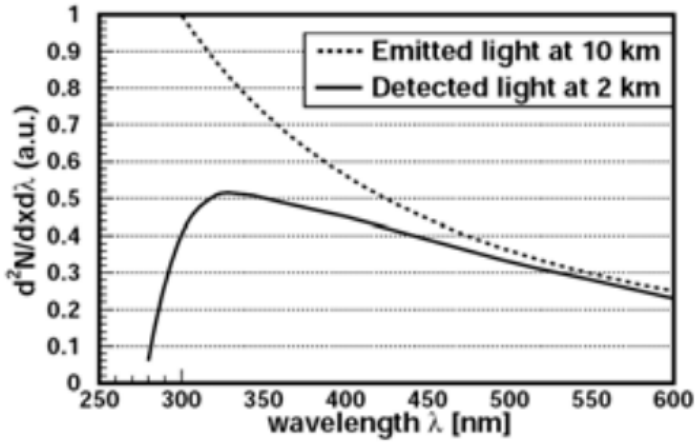

Figure 5. Spectrum of Cherenkov light at the shower maximum (dashed curve) and after traveling down to 2 km altitude (full curve). [1]

Most of the Cherenkov photons are emitted at short wavelengths, in the ultraviolet range and the number of photons emitted decreases along the visible region Figure 5. Due to atmospheric interaction, especially ozone absorption, detectable light shows an energy peak at around 330 nm.

1.3. Extensive Air Shower (EAS)

Gamma rays are very energetic, so when they interact with the atmosphere (it usually starts at 20km above the sea level) they can create pairs of electrons and positrons by pair production (Figure 6). These new pair of charges can produce high energy gamma rays by the Bremsstrahlung process.

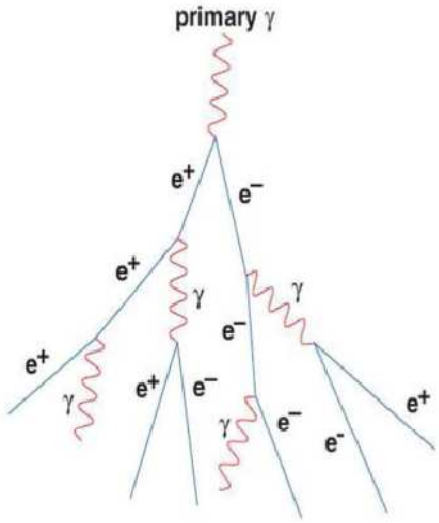

Figure 6. Electromagnetic air shower development scheme.

The produced gamma photons can go on to produce more electrons and positrons starting a cascade process called Extensive Air Shower (EAS) that last until the EAS energy is completely absorbed by the atmosphere.

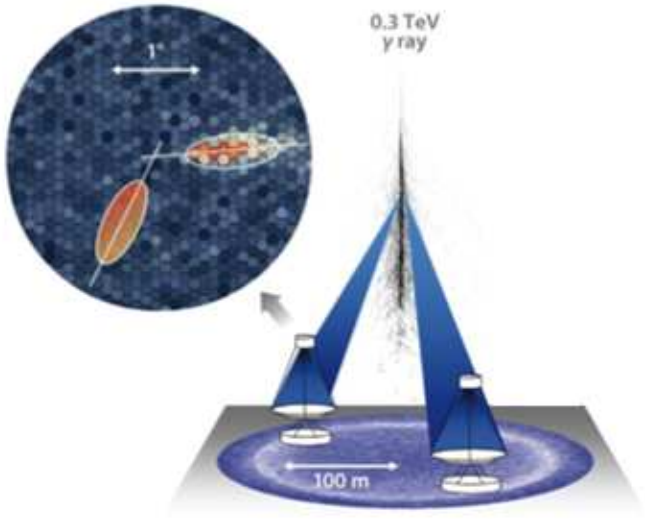

Figure 7 Sketch of the Imaging Atmospheric Cherenkov Technique (IACT). The Cherenkov light produced by an EAS is collected by two IACTs and the two images are combined to determine the direction of the primary (stereo technique) [2].

Each particle of the shower produces Cherenkov radiation. This radiation propagates within a cone that describes a circle or ellipse on the ground, called

light pool. If a telescope is located inside this foot print, it could detect the shower (Figure 7). The size of the light pulse is just a geometrical projection and does not depend on the energy of the cosmic ray. However, the energy of the gamma ray can be determined by the density of Cherenkov photons.

1.4. Atmosphere interaction

The atmosphere is a layer of gases surrounding the planet Earth that is retained by Earth's gravity. The whole atmosphere reaches up to 10.000 km above the surface of the earth and it is mainly composed by Nitrogen (N2 ~78%), Oxygen (O2 ~21%), Argon (Ar <1%) and other minor species.

By convention, the atmosphere is divided into layers according to the variation of temperature with the height (Figure 8). These layers are:

- **Troposphere**. It is the lowest layer and extends from the ground up to 10km at the pole and 20km at the equator. 75% of the total mass of the atmosphere is contained in this layer.

- **Stratosphere**. It extends from 20 km up to 50 km and contains 24% of the atmosphere mass. The end of this layer can be considered as the beginning of space. At this high, the formation of clouds is very rare.

- **Thermosphere**. It contains fewer molecules and ranges from 90 up to 600 km.

- **Exosphere**. Above 600km, it contains occasional molecules gradually escaping into space. From this height artificial satellites can be found.

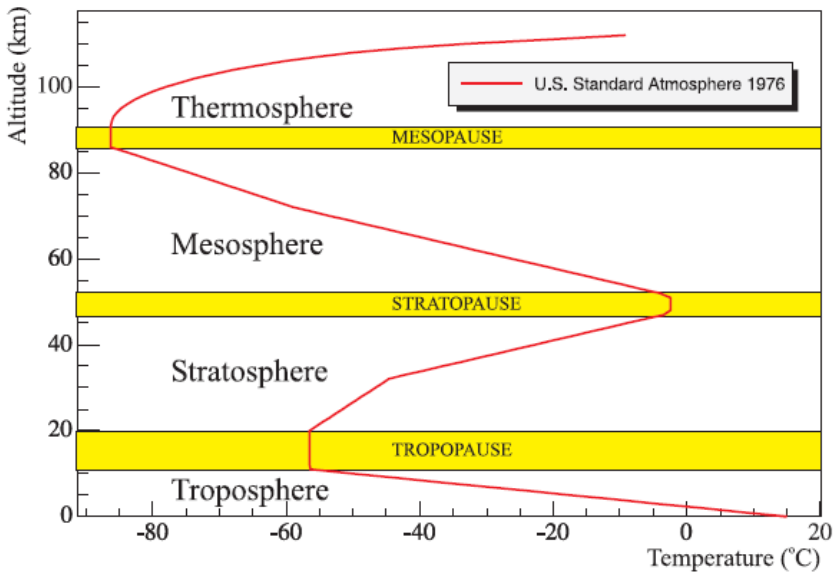

Figure 8.Typical vertical structure of atmospheric temperature. Data from U.S. Standard Atmosphere 1976 (NASA). [3]

Extensive Air Shower takes place in the Troposphere. The behavior of the lower layer of the atmosphere is directly influenced by its contact with planetary surface defining the Planetary Boundary Layer (PBL). Within this sublayer (considered up to 3 km [4] [5]) aerosols, as for example pollen, dust, water droplets, sea salt or smoke, are in suspension.

When light goes through the atmosphere it interacts with gas molecules and aerosols scattering a portion of the incident radiation in all directions and changing its spatial distribution. Two possible types of scattering can occur depending on the wavelength of the incident light and the scattering body size:

- Rayleigh scattering occurs when the particles causing the scattering are smaller than the wavelength of the incident light. When it comes to Cherenkov radiation, this mainly happens with atmospheric gases.

- Mie scattering might be caused by aerosols as their size is larger than the Cherenkov radiation wavelengths.

Besides scattering, absorption is another process that takes place when light interacts with the atmosphere. In the UV region, absorption processes are dominant but from 300 nm, the atmosphere can be considered absorption free [3].

1.5. Structure of the thesis and main goals

The Institute for High Energy Physics (Institut d'Altes Energies, IFAE) is a consortium between the government of Catalonia and the Universitat Autònoma de Catalunya (UAB). Since it was created in 1991, IFAE conducts experimental and theoretical research in Particle Physics, Astrophysics and Cosmology. Among other projects, IFAE was involved in the design and construction of MAGIC telescopes and it is currently designing the Cherenkov Telescope Array.

The current generation of IACTs like MAGIC makes only simplistic checks of the atmospheric transparency to reject bad quality data. These systems are highly dependent on the atmosphere conditions in every measurement. Furthermore, the energy of EASs is detected with an error of 20-30%. This is why IFAE and UAB work together developing a Raman LIDAR. This instrument is capable of characterizing the atmosphere describing a vertical profile of aerosols and molecules. This information will help to correct the data captured from IACTs that is currently being rejected, due to its bad quality. It will also allow the improvement of data resolution.

A LIDAR is basically a system composed by a LASER which emits pulses to the atmosphere, a telescope to collect the backscattered light, and some units to adapt the received light and process the information. The LIDAR will be placed next to the MAGIC telescope and take measures towards the same point in the sky.

Some atmospheric simulations show that in order to correct data from IACTs, measurements should be taken up to 10-12 km high in the atmosphere, especially when it comes to aerosols [1] [6]. Furthermore, it is necessary that the measurements done in the atmosphere are always range-resolved and that is exactly what LIDAR guarantees.

As the scattering process depends on the size of the particles and the incident wavelength, the characterization must be done for that same wavelength range where Cherenkov light takes place. This situation forces the use of LIDAR to take measurements when the IACTS are not working. Otherwise data will be corrupted by the laser light.

The LIDAR is to work as a cooperative atmospheric calibration instrument that takes measurements while IACT's change their position in order to start scanning another part of the sky. This switching time is around 1-2 min and measurements longer than 5 minutes are not desirable.

In this document, the preliminary design of the IFAE-UAB Raman LIDAR is presented, which fits the requirements above. **Chapter 2** reviews a brief introduction to LIDARs and tackles the estimation of received power, Signal-to-Noise Ratio (SNR), and the observation time needed by the LIDAR system to take measures. **Chapter 3** focuses on the IFAE-UAB Raman LIDAR power link budget and a discussion about its components. **Chapter 4** presents a proposal for the optic design of the polychromator unit. Finally, **Chapter 5** summarizes conclusions and future recommendations. Finally, this work has given rise to a paper (contained in the **Annex**) to be submitted to MNRAS (Monthly Notices of the Royal Astronomical Society, IF=5.185) as a joint collaboration effort among IFAE, UAB and UPC institutions.

Chapter 2. Concept design of the IFAE-UAB Raman LIDAR

This chapter presents a brief introduction to the LIDAR technique, its history and its main uses. Also, a description of the opto-atmospheric model used is given and the formulation of the power link budget and the observation time needed in every LIDAR measurement.

2.1. The LIDAR technique

LIDAR (Light Detection And Ranging) is an optical remote sensing technique analogous to the RADAR principle. Mainly, it is based on a laser which emits light pulses to the atmosphere, a telescope which collect the backscattered light, a polychromator unit where the light is distributed to the sensors and a recorder unit. Since light travels at a known speed, the atmosphere can be characterized in range from the time delay from the pulse emission to its reception.

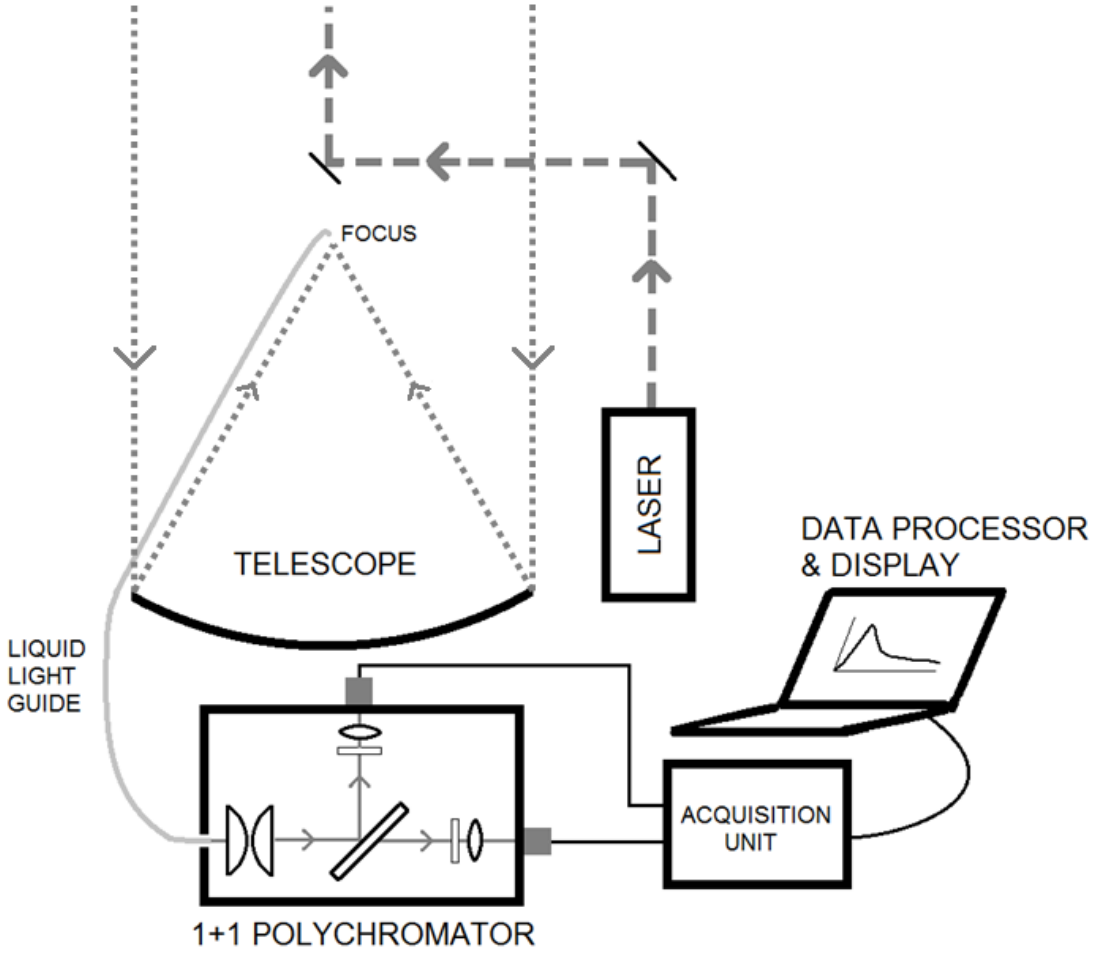

Figure 9. Schematic of the IFAE-UAB LIDAR system

LIDAR belongs to the remote sensing family techniques. Bats make use of a perceptual echolocation system by the emission of ultrasonic sounds. They compare returning echoes with the outgoing pulses and they are able to reproduce images of surroundings from them. During the 1930s the first invention based on this principle appeared, the SONAR, and it was used for underwater detection. A few years later, during World War II, the RADAR system was developed by the British to protect their borders, by means of microwaves capable to detect targets at large distances.

The use of light for detection dates back to the 1930s, where searchlights were used to measure air density profiles. Also, in 1938, cloud base heights were measured by means of pulses generated by flashlamps. The first LIDAR system appeared in the 1960s [7] and was used to measure of Lunar to Earth distance. It was one of the first times the revolutionary invention of the LASER was used.

In the 1970s, NASA started doing research about airborne LIDAR prototypes for eventual space borne sensor deployment. But, it was only with the deployment of Global Positioning Systems (GPS), ten years later, that an accurate positioning of the aircraft made the airborne surveying possible. From this time, numerous airborne and space borne missions incorporate LIDAR systems. Also ground based observations made use of this technique like in the EARLINET project [8], a network of LIDAR ground bases for aerosol observation at continental scale.

Usage of a LIDAR

When the laser beam interacts with the atmospheric components (aerosols and molecules), the light is scattered in all directions. A small part of this light is scattered back to the telescope and collected. Nowadays, the analysis of these data is useful in many fields as for instance in cartography, topography, agriculture, forestry, archeology and pollution modeling, as well as in navigation systems or police laser speed detectors [9].

In the last years several technologies have raised besides the pure use of elastic LIDARs. By the time of this paper, the main techniques are following:

Elastic LIDAR is the simplest technique and provides information about the atmosphere constituents, aerosols, clouds, etc. The word ‘elastic’ stands for the interaction with particles and molecules where the incident and backscattered light have the same wavelength.

Inelastic Raman LIDAR is usually employed parallel to elastic LIDAR measurements. When the light interacts with molecules, part of this light is backscattered with a wavelength shift characteristic of every type of molecule. By analyzing this returned power it is possible to determine the gas concentration in range. It is also possible describe the temperature of the atmosphere in range measuring the inelastic returned power.
Differential Absorption LIDAR (DIAL) is used for measurement of gas concentration such as ozone, carbon dioxide or water vapor. DIAL

measurements rely on the unique “fingerprint” absorption spectrum of each molecule. Two measurements are made, one at wavelength where the gas under study presents a peak of absorption, and a second at wavelength in the region of low absorption. The differential absorption between two wavelengths gives the concentration of the gas as a function of range.

Doppler LIDARs are used for wind speed and direction measurements. The idea is the same as in the Doppler RADAR, that makes use of frequency shifts of the backscattered signal to determine the speed of the target. LIDARs do not operate with radio wavelength but with shorter wavelengths. In that way, RADARs are sensitive for larger targets such as rain drops or birds, while LIDARs are sensitive to aerosol particles.

Inelastic interaction. The Raman LIDAR technique

The fraction of light scattered by an element towards the light source will be called from now on backscattered light. As the light goes on through the atmosphere, it scatters continuously and the transmitted light becomes weaker and weaker. This last fact will be referred along this document as the extinction of the light.

LIDARs can provide range-resolved profiles of the backscatter and extinction coefficients needed to characterize the atmosphere. These coefficients depend on the significant spatial variation in the particle composition and size distribution, especially in the Planetary Boundary Layer (PBL). The problem of extracting the backscatter and extinction coefficients from one measurement can be overcome taking independent measurements with a Raman LIDAR along the line of sight of the elastic LIDAR.

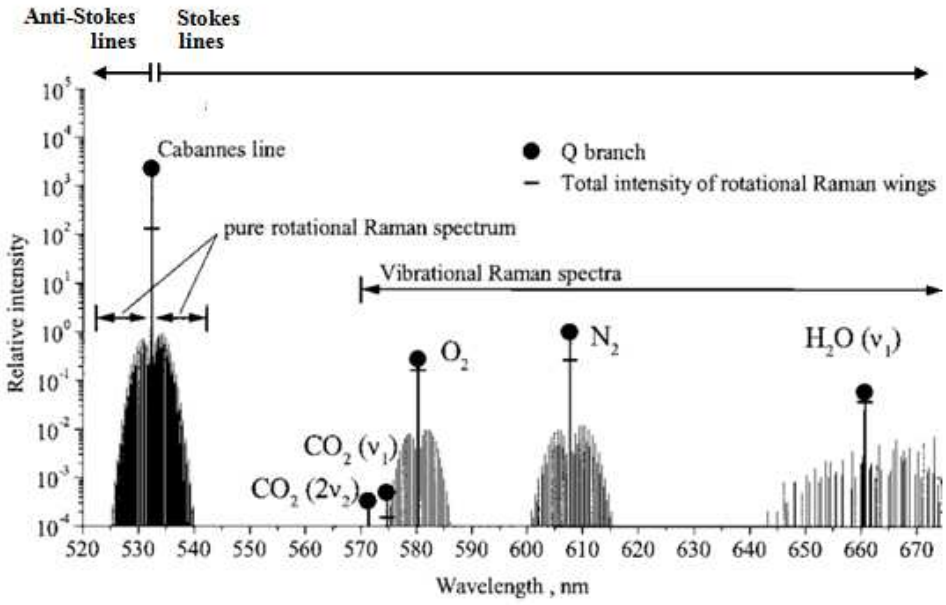

Figure 10. Overview of lidar backscatter signals for a laser wavelength of 532 nm. Adapted from [10].

The Raman LIDAR technique has turned out to be a very stable and reliable tool thanks to the improvements achieved in the interference filters and high power lasers over the last years [11]. It makes use of the weak inelastic scattering of light by atmospheric molecules. When molecules are exposed to a light source, different rotational and vibrational molecular energy levels are excited. This excitation changes the quantum state of a molecule and shifts the frequency of the scattered photon. The spectrum plotted by Raman lines for an excitation wavelength of 532 nm can be seen in Figure 10.

If a high energy level is excited, the molecule absorbs energy and the frequency of the scattered photon is decreased. Inversely, the wavelength is increased. The former inelastic process is called Stokes Raman scattering. In contrast, if the energy level is lower the molecule transfers this energy to the scattered photon decreasing its wavelength. These processes are called the anti-Stokes lines. The unshifted return from the laser is the Cabannes line, which concentrates the highest power.

Every Raman band or signal is characteristic of every type of scattering molecule. Their central line is called Q branch and the power concentrated at this spectral line is several orders of magnitude higher than their side bands.

There has been much research on this field, and many applications that filter and use different parts of the cited spectrum have been developed. For example, measurements of atmospheric temperature are possible by analyzing the pure rotational Raman spectrum, which are the side bands around the Cabannes line.

Raman process results in a frequency shift of the laser wavelength depending on the aerosol under study. Nitrogen has been used in all the Raman application because it is the major atmospheric component. The returned power after the nitrogen Raman scattering when it is exited by a λ_0 wavelength light source is given at the wavelength

$$\lambda_R = \frac{\lambda_0}{1 - \lambda_0 \cdot \kappa}, \qquad (1)$$

where κ is the wavenumber (2331 cm^{-1} for N_2) [12]. The IFAE-UAB Raman lidar will take measurements from the elastic and Nitrogen Raman scattering return. From here on we will assume that the Raman channel is centered at the wavelength λ_R equal to 387 nm and λ_0 and stands for the source wavelength 355 nm.

2.2. Power link budget

In a lidar, a train of light pulses is emitted into the atmosphere, the telescope collects the scattered light in the same direction and the data are processed after the detector. In between, different subsystems such as the light guide, lenses, detectors or the even transient recorders take an important role in determining the figure of merit of the whole system. The estimation of the

received power and signal-to-noise ratio can be useful in the appropriate selection of the different devices and provides information about the maximum range, spatial resolution and the observation time needed for the measurements.

2.2.1. Opto-atmospheric parameter modeling

Elastic received power is produced by both molecular and aerosol scattering while the Raman received power is produced only by molecular interaction with the molecule of interest and therefore molecular scattering. Nevertheless, light propagation is always affected by extinction processes due to the interaction with molecules and particles.

In order to estimate backscattering and extinction coefficients we have assumed a standard atmospheric model for the aerosol and molecular components hereafter described:

Aerosol component (Mie scattering)

A very simple wavelength dependent model has been taken for Mie backscattering processes in which aerosols are homogeneously distributed up to the Planetary Boundary Layer (PBL, considered here at 3km). Beyond the PBL, a purely molecular atmosphere is considered. Extinction component is computed from Koshmieder's relationship [13]

$$\alpha_{aer}(532nm) = \frac{3.912}{VM}[Km^{-1}], \quad (2)$$

being VM the Visibility Margin and for clear sky, that for the reference wavelength of 532 nm is approximately 39.12 Km [14]. From here on, indexes 'aer' and 'mol' stand for aerosol scattering and molecular scattering respectively. The extinction coefficient is scaled to the wavelength of interest λ_i, whether 355 nm or 387 nm, using the equation (3). k is the Angström coefficient which has been considered unitary [15].

$$\alpha_{\lambda_i}^{aer} = \left(\frac{\lambda_i}{\lambda_{532}}\right)^{k} \alpha_{\lambda_{532}}^{aer} \quad (3)$$

The aerosol elastic backscattering coefficient is related to the aerosol extinction coefficient by

$$\beta_{\lambda_0}^{aer} = \frac{\alpha_{\lambda_0}^{aer}}{S_M}[Km^{-1}sr^{-1}], \quad (4)$$

where S_M is the lidar ratio. Extracted from the look-up table of [14], S_M is around 25.

Molecular component (Rayleigh scattering)

The molecular height-dependent extinction coefficients have been simulated by using an atmospheric model provided by the RSlab department of UPC, based on the U.S. standard atmospheric model [16] which is defined for a 'standard air' [17]. This model accounts for the height dependent refractive index and the dry-air molecular number density. The molecular elastic backscattering coefficient is given by the Rayleigh ratio

$$\beta_{\lambda_0}^{mol}(R) = \frac{3}{8\pi}\alpha_{\lambda_0}^{mol}(\mathrm{R}) \ , \qquad (5)$$

On the other hand, the inelastic Raman scattering is only produced by the species under study so that the inelastic backscattering coefficient depends on the nitrogen molecular number density, which is about 78% of the dry-air molecular number density.

The inelastic backscattering coefficient can be written as

$$\beta_{\lambda_R}^{mol}(R) = N_{N_2}(R)\frac{d\sigma_{\lambda_R}(\pi)}{d\Omega} \ , \qquad (6)$$

where N_{N_2} is the N_2-molecule number density depending on height, $d\sigma_{\lambda_R}(\pi)/d\Omega$ is the N_2-Raman backscattering differential cross-section ($23.15\cdot10^{-35}$ [m^2sr^{-1}] at 387 nm). The molecular scattering cross section is proportional to λ^{-4} [11] and this is the mean reason why usually small emission wavelengths are preferred. Finally, Mie and Rayleigh extinction coefficients for elastic and inelastic processes are plotted in Figure 11.

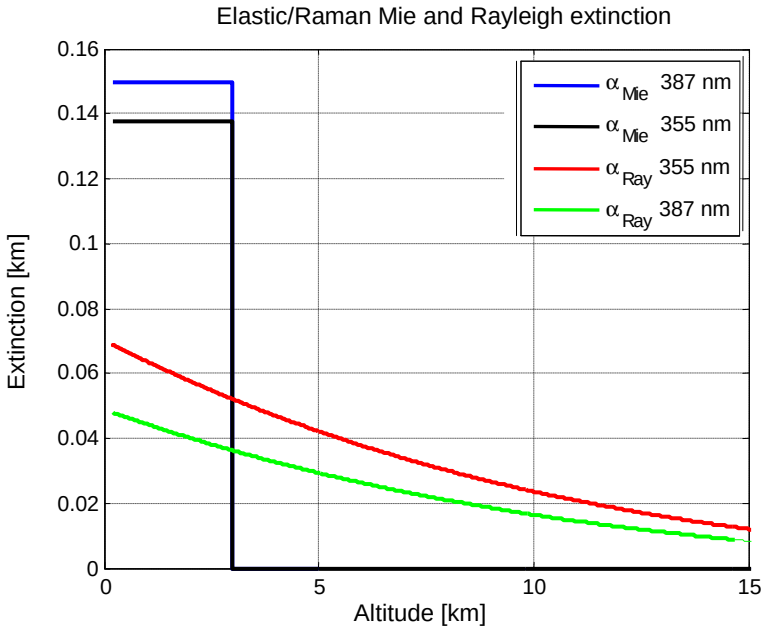

Figure 11. Simulated range dependent aerosol (Mie) and molecular (Rayleigh) extinction coefficients.

2.2.2. Elastic received power

In the elastic Mie/Rayleigh backscattering, the received power is given by the LIDAR equation

$$P_{\lambda_0}(R) = \frac{K}{R^2}\left[\beta_{\lambda_0}^{mol}(R) + \beta_{\lambda_0}^{aer}(R)\right] e^{\left[-2\int_0^R \alpha_{\lambda_0}^{\mathrm{mol}}(\mathrm{r}) + \alpha_{\lambda_0}^{\mathrm{aer}}(\mathrm{r})dr\right]} OVF_{\lambda_0}(R), \qquad (7)$$

where K is the range independent system constant which can been written as $K = \frac{E\,c}{2} A_r$. E is the pulse energy emitted by the laser, c is the speed of light, A_r is the area of the telescope, $\beta_{\lambda_0}^{mol}(R)$ and $\beta_{\lambda_0}^{aer}(R)$ are the backscatter coefficients and $\alpha_{\lambda_0}^{mol}(R)$ and $\alpha_{\lambda_0}^{aer}(R)$ are the extinction coefficients as a function of distance for the emitted pulses wavelength.

$OVF(R)$ is the overlap factor; it is a relative magnitude which expresses how well the telescope "sees" the beam of the laser for any range R and it has been considered to be 1 since the configuration laser beam-telescope axis is coaxial. Figure 12 shows full overlap along the whole range when the telescope field of view is greater than the laser divergence in a co-axial system. Also a bi-axial LIDAR is showed for comparison.

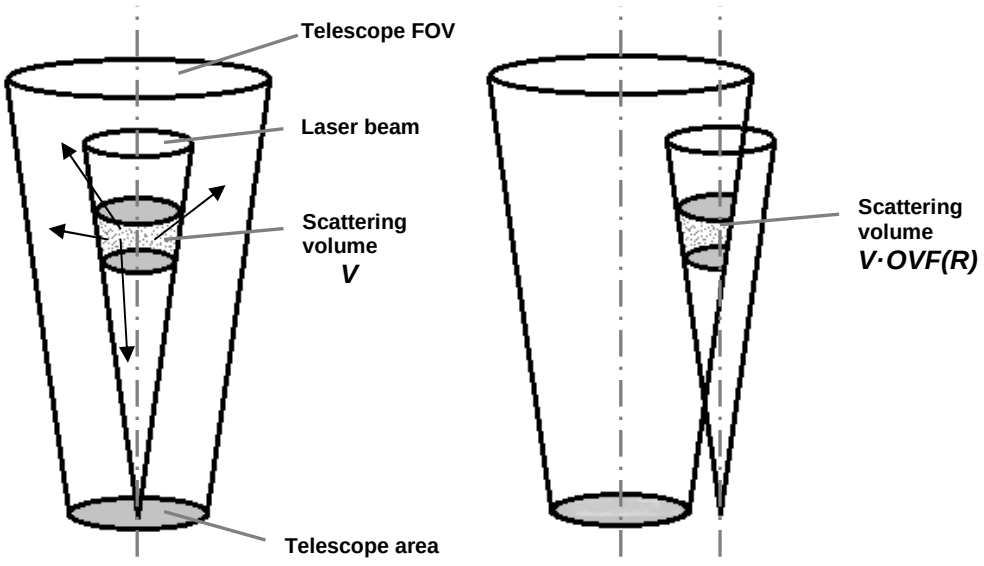

Figure 12. Schematic of co-axial LIDAR (a) and bi-axial LIDAR (b)

The measured power at range R depends on the sum of the molecular and particle backscattering coefficient. The exponential term of the equation is called the transmittance and the factor two is due to the two-way path extinction that takes place along the round-trip path from the light source to the scattering element and back to the telescope.

2.2.3. Raman received power

Analogously, the received power in the Raman channel can be written as

$$P_{\lambda_R}(R) = \frac{K}{R^2}\beta_{\lambda_R}^{mol}(R)\, e^{-\int_0^R\left[\alpha_{\lambda_0}^{mol}(r)+\alpha_{\lambda_0}^{aer}(r)+\alpha_{\lambda_R}^{mol}(r)+\alpha_{\lambda_R}^{aer}(r)\,dr\right]} OVF_{\lambda_R}(R), \quad (8)$$

where K is the system constant. $OVF(R)$ is the overlap factor and it is unitary along the whole range R since the co-axial configuration of the LIDAR. The backscattering and extinction coefficients are computed in the previous section. In contrast with the elastic received power, Raman process is produced only by molecules and it just depends on the inelastic backscattering coefficient (equation (6)). Furthermore, the light extinction takes place in different wavelengths in the round trip. LASER light (at 355 nm) is extinguished by molecules and aerosols ($\alpha_{\lambda_0}^{ray}(r)$ and $\alpha_{\lambda_0}^{mie}(r)$) along its way. After being backscattered by the nitrogen at the distance R and at 387 nm, it returns to the telescope being again extinguished by both molecules and aerosols ($\alpha_{\lambda_R}^{ray}(r)$ and $\alpha_{\lambda_R}^{mie}(r)$).

2.2.4. Background received power

The function of the telescope is to collect the laser light backscattered in the atmosphere. But even when the laser is off, the telescope collects light from the sky. The power received in such condition is called background power and it should be lower than the signal light. It has been a challenge for daytime Raman LIDARS but high power lasers and very narrow filters developed in the last years have overcome this problem. The background power is given by

$$P_{back}(\lambda) = L_b A_r d\Omega d\lambda, \quad (9)$$

where L_b is the irradiance from the sky, A_r is the telescope area, $d\Omega$ is the solid angle computed from the telescope field of view and $d\lambda$ is the interference filter bandwidth in every channel. For the case of the IFAE-UAB lidar, the elastic and Raman channel have the same filters and thus they receive the same background power.

The Raman LIDAR that is under development will work in La Palma solely at night. For that reason, the irradiance of the night sky was measured in [18] and is $2.72 \cdot 10^{-13}$ [$W \cdot cm^{-2} \cdot nm^{-1} \cdot sr^{-1}$]. The LIDAR will be always pointing at different directions in the night sky but under no circumstances towards the moon. That will decrease significantly the power received from the background simplifying the design of the system.

2.2.5. Channel transmissivity

The channel transmissivity ($0 \le \xi \le 1$) is defined as the product of the individual subsystem transmission factors (i.e., the inverse of the optical losses) along the optical receiving chain. Formally,

$$\xi(\lambda) = \xi_T(\lambda)\xi_{PSF}(\lambda)\xi_g(\lambda)\xi_{poly}(\lambda), \tag{10}$$

where $\lambda = \lambda_0, \lambda_R$ is the elastic/Raman reception wavelength, $\xi_T(\lambda)$ is the telescope transmission, $\xi_g(\lambda)$ is the liquid-guide transmission, $\xi_{PSF}(\lambda)$ is the guide-to-telescope coupling efficiency due to the PSF of the telescope (Sect. 3.2), and $\xi_{poly}(\lambda)$ is the total polychromator transmission defined as

$$\xi_{poly}(\lambda) = \xi_{dichr}(\lambda)\xi_{lens}(\lambda)^n \xi_{IF}(\lambda), \tag{11}$$

where $\xi_{dichr}(\lambda)$, $\xi_{lens}(\lambda)$, and $\xi_{IF}(\lambda)$ are the dichroic mirror (D1), lenses (L1-L4), and interference-filter transmission factors, respectively, described later in Table 4 Section 4.1 . In Equation (11), $n = 3$ for all the lenses (L1-L4) in each channel of the polychromator are assumed identical transmissivities. The elastic/Raman channel transmissivities, according to Equation (10), are listed in Table 1 along with the channel voltage responsivity (or net voltage responsivity),

$$R_v'(\lambda) = R_i(\lambda)G_T\xi(\lambda), \tag{12}$$

defined as the product of the current responsivity of the detector, R_i [A/W], times the transimpedance gain G_T ($G_T = R_{in} = 50\Omega$, i.e., the input impedance of the transient recorder), times the channel transmissivity, $\xi(\lambda)$ from (10) above.

2.2.6. Signal-to-noise ratio

Every element in the system can act as a noise source, resulting in a bad detection of the light received. But some of these are more relevant than others, thus limiting the LIDAR performances. In these systems the predominant noise comes usually from the photomultiplier tube (PMT).

When light enters the photocathode (the sensitive part of the PMT), electrons are emitted and multiplied by a secondary electron emission through the dynodes, and these are collected by the anode as an output pulse. If incident light is strong, these pulses are so close in time that the processing circuit is not fast enough and they overlap creating an analog current with shot noise fluctuations [19]. In this situation, the only way to analyze this continuous current is by using what is known as *Analog Mode*. In contrast, when the light intensity is weak, pulses are detected individually. Since detected pulses

undergo binary processing for digital counting, this method is known as *digital mode* or *photon-counting mode*.

Inelastic received power is around 3 orders of magnitude lower than the elastic one, due to the low cross sections of Raman scattering. That is the reason why Raman LIDARs need high power lasers, large telescopes, long integration times and they are mostly used for gases with high molecular concentrations. The results given in this paper assume analog detection for the elastic channel and photon counting mode for the Raman channel whilst the acquisition module records both at the same time. Depending on the energy level of the signal it is used digital or analog data, and in the region in between the system uses a "gluing" algorithm that can increase the final SNR.

Signal-to-noise ratio for the elastic channel

As stated before, the *Analog Mode* is used when the photons flow reaching the photocathode is so intense that the output pluses at the anode overlap and produce a continuous current with noise fluctuations. Shot noise is basically caused by 3 sources:

- Shot Noise Resulting from Signal Light: Since the secondary electron emission in a photomultiplier tube occurs with statistical probability, the resulting output also has statistical fluctuation.

- Shot Noise Resulting from Background Light: It is generated in the same way as the shot noise resulting from the signal light.

- Shot Noise Resulting from Dark Current: Even when there is no light entering the photocathode an output current is observed. This dark current is mainly caused by thermionic emission from the photocathode and dynodes.

These three noise components and the thermal noise added by the acquisition unit have associated noise spectral densities that can be computed as

$$\sigma_{sh,s}^2(R) = 2qG_T^2FM^2R_{io}P(R)\xi \left[\frac{V^2}{Hz}\right], \quad (13)$$

$$\sigma_{sh,b}^2 = 2qG_T^2FM^2R_{io}P_{back}\xi \left[\frac{V^2}{Hz}\right], \quad (14)$$

$$\sigma_{sh,d}^2 = 2qG_T^2FM^2I_{db} \left[\frac{V^2}{Hz}\right], \quad (15)$$

$$\sigma_{th}^2 = 4kTR_{in} \left[\frac{V^2}{Hz}\right], \quad (16)$$

where G_T is the transimpedance channel gain [V/A] (i.e., the acquisition unit input impedance, $G_T = R_{in} = 50\Omega$), F is the photomultiplier excess noise factor [dimensionless units], M is the PMT multiplication factor or gain, R_{io} is the cathode radiant sensitivity [A/W], $P(R)$ is the return power [W], P_{back} is the background-radiation power [W], ξ is the net optical transmissivity [dimensionless units], I_{db} is the bulk-dark current [A], q is the electron charge [C], k the Boltzmann's constant [J/K] and $T = 300\mathrm{K}$ is the noise equivalent temperature.

These variances are expressed as noise spectral density and they have to be multiplied by the noise equivalent bandwidth B_N= 10 [MHz] to compute the SNR. Then the signal to noise ratio takes the form

$$SNR_a(R) = \frac{R_{io} M G_T \xi P(R)}{\sqrt{[2qG_T^2 F M^2 R_{io} \xi [P(R) + P_{back}] + 2qG_T^2 F M^2 I_{db} + 4kTR_{in}]B_N}} \left[\frac{V}{V}\right] \quad (17)$$

Then, if the thermal noise is much lower than the other noise sources it is safe to conclude that the SNR does not depend either on the multiplication factor of the PMT or on the transimpedance channel gain since they cancel out in the equation (17) .

Signal to noise ratio for the Raman channel

Photon counting mode is used when the number photons entering into the photocathode is so low that output pulses can be detected as separate pulses. In this mode we find the same three noise sources as the ones in the analog mode, but variances are computed in counts per second. They can be computed as

$$\mathrm{N_{ph}} = \mathrm{P_{ram} L_r R_{io}/q\ [counts/sec]}, \quad (18)$$

$$\mathrm{N_b} = \mathrm{P_{back} L_r R_{io}/q\ [counts/sec]}, \quad (19)$$

$$\mathrm{N_d} = \mathrm{I_{db}/q\ [counts/sec]}, \quad (20)$$

where $\mathrm{N_{ph}}$ is the number of photo-induced counts from signal light per second, $\mathrm{N_b}$ is the number of photo-induced counts from the background light per second and $\mathrm{N_d}$ is the number of photo-induced counts from the dark-current per second. Then the SNR in photon counting mode is

$$\mathrm{SNR_{pc}(R)} = \frac{\mathrm{N_{ph}(R)}\sqrt{\tau}}{\sqrt{\mathrm{N_{ph}(R) + 2(N_b + N_d)}}}, \quad (21)$$

where τ the fraction of time is where the photo-counter is adding counts (considered 100 ns to achieve the same spatial resolution than in *Analog Mode*)

2.2.7. Integration time

As it has been discussed in Chapter 1, the goal of building this LIDAR is to improve the quality of data taken with ground-based Cherenkov telescopes. They work independently and the Raman LIDAR should not interfere with astronomical data acquisition, that can be achieved by using the dead time between two subsequent measurement campaign when the telescopes is repointing. The integration time is the time needed for the LIDAR in one observation to get the necessary SNR. Thus, this time turns into a key parameter in trade-off with the maximum range.

Pulse integration is commonly used in many detection systems to improve the signal received, by degrading the range resolution. When N pluses are integrated, the signal to noise ratio is improved by square root of N. Thus, the number of pulses to integrate is

$$N = \left\lceil \frac{SNR_{goal}}{SNR_{\simeq}} \right\rceil^2 \tag{22}$$

where $SNR_{\simeq}$ is the signal to noise ratio of a single pulse, SNR_{min} is the minimum needed signal to noise ratio and N must be a rounded up integer. Then, the observation time needed to integrate enough pulses to fulfill the detection condition is

$$t_{obs} = \frac{N}{PRF} \tag{23}$$

And equivalently using equations (22) and (23)

$$t_{obs} = \left(\frac{SNR_{goal}}{SNR_{\simeq}}\right)^2 \cdot \frac{1}{PRF} \tag{24}$$

where SNR_{goal} is the minimum Signal-to-Noise Ratio required by the inversion algorithm used, which will be defined at a later time of the project. In our case a ratio of 10 has been used. To stand out the importance of the inversion algorithm, Figure 13 shows the observation time needed versus range. For the same LIDAR system, two different inversion algorithms are considered in this plot, being the related SNR_{goal} equal to 1 (blue line) and equal to 10 (red line). The SNR needed is increased a factor of 10, resulting in an increase of the observation time by a factor of 100 for the same range. With this implication, a system that normally needs a few seconds to take measurements would need a few minutes if a different algorithm is used.

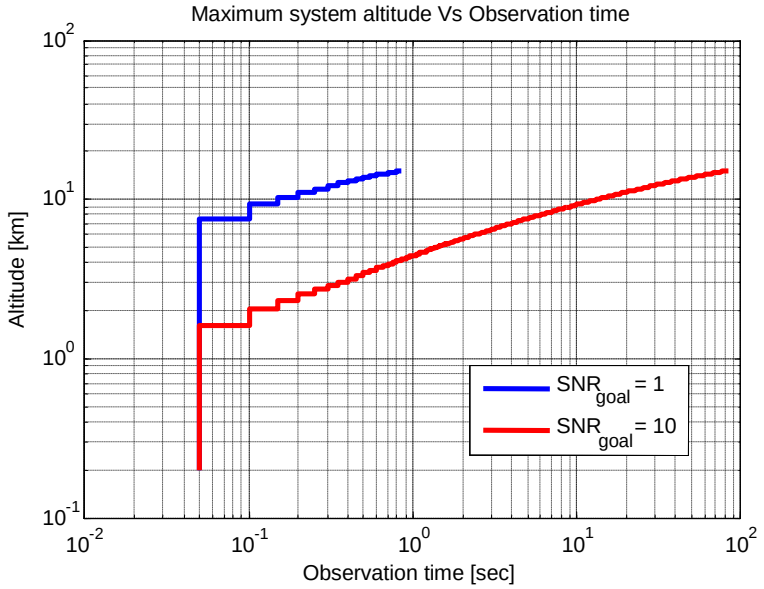

Figure 13. Lidar altitude versus observation time for SNR goal equal to 1 and equal to 10

In a similar way, any improvement in the SNR by a factor of ζ reduces the observation time a factor of ζ^2 as this

$$t_{obs}' = \frac{N}{PRF} = \left(\frac{SNR_{goal}}{\zeta \cdot SNR_{\hat{=}}}\right)^2 \cdot \frac{1}{PRF} \qquad (25)$$

or in short

$$t_{obs}' = \frac{t_{obs}}{\zeta^2} \qquad (26)$$

From here on, all the simulations are made with a SNR_{goal} equal to 10. If it is improved in the inversion stage, the observation times given in this document can be recomputed easily with the equation (21).

2.3. Performance assessment of the IFAE-UAB LIDAR

The power link budget of our LIDAR consists on the range-resolved computation of the received power. This is useful to evaluate the optical losses of the system, the SNR at the receiver, the observation time needed to take atmospheric measurements up to a desired range and how the different components of the LIDAR affect the performance.

EMITTER		
LASER	Type Model Emitted wavelength, λ Energy per pulse, E Pulse Repetition Frequency, PRF Beam waist (diameter) Beam Divergence, θ Pulse duration, τ_p	Nd:YAG Quantel Brilliant 355 nm 60 mJ 20 Hz 6 mm 0.5 mrad 5 ns
RECEIVER		
Telescope	Geometry Diameter, d Shadow diameter, d_{sh} Focal length, f Transmissivity, ξ_T	Parabolic mirror 1.8 m 0.08 m 1.8 m 0.55
	Liquid-guide-to-telescope coupling efficiency, ξ_{PSF}	0.9
Liquid Guide	Manufacturer & Model Active area diameter, d_b Numerical Aperture, NA Transmissivity, ξ_g	Lumatec Series 300 8 mm 0.59 (34º half-angle) >0.7 (in the UV)
Photodetectors	Type Active area diameter, d_b PMT model	PMT 22 mm Hamamatsu R1924A
Acquisition unit (transient recorder)	Type Model	Mixed analog-to-digital converter (ADC) / Photon counter (PC) ADC 20 Msps 12bit / 250-MHz PC LICEL TR20-160
CHANNEL SPECIFICATIONS		
Wavelength [nm]	355	387 (N_2)
Type	Elastic	Raman
Resolution [m]	Up to 15 m in analog mode (10-MHz bandwidth), up to 7.5 m in photon-counting mode (50-ns bin)	
Polychromator TX, ξ_{poly} (Eq.(11))	$0.90\times0.90^3\times0.60 = 0.39$	$0.90\times0.90^3\times0.65 = 0.43$
Channel transmissivity, ξ_{poly} (Eq.(11))	0.15	0.16
Channel responsivity, R_v' [V/W]	8.0×10^5	8.7×10^5
Spectral Bandwidth, $\Delta\lambda$ [nm]	10	10
Type of Detector	PMT	PMT
Model	R1924A (Hamamatsu)	R1924A (Hamamatsu)
Transimpedance gain (input impedance of the transient recorder) [Ω]	50	50
Internal Gain, M	$2x10^6$	$2x10^6$
Noise Factor, F	1.8	1.8
Current responsivity, R_i [A/W]	$1.1x10^5$	$1.1x10^5$
Dark current, I_d [nA]	3	3

Table 1. Specifications of the lidar system

To evaluate the equations exposed in Chapter 2 we have programmed a MATLAB script. The plots simulated in this chapter illustrate the importance of the subsystem parameter choice in the link budget. Table 1 shows the parameters of the IFAE-UAB LIDAR.

The received power in the elastic and Raman channel is showed in Figure 14, as well as the power received from the background; computed with equations **(7)**, **(8)** and **(9)**. Thus proving, that background power is about two orders of magnitude lower than the Raman received power at 15km.

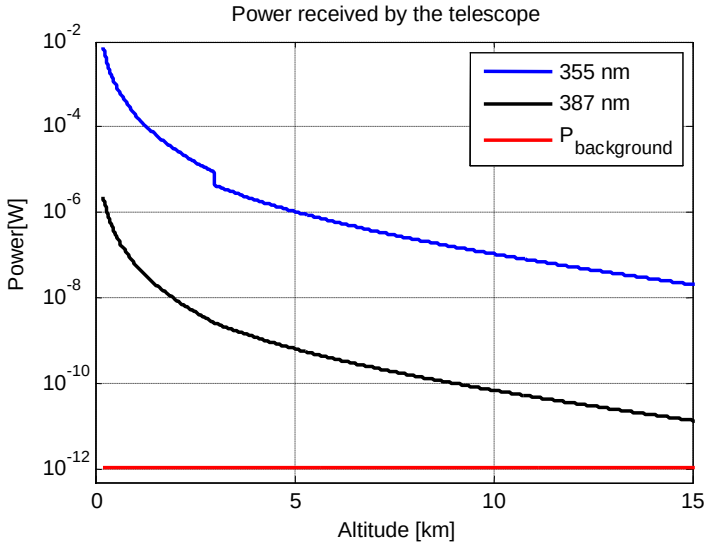

Figure 14. Received Power versus altitude

Figure 15(b) shows that signal shot noise variances in the elastic and Raman channel are above other noise variances. This is due to the large size of the telescope and the low irradiance of the night sky, and therefore the system will be dominated by signal shot noise minimizing the role of other noise sources.

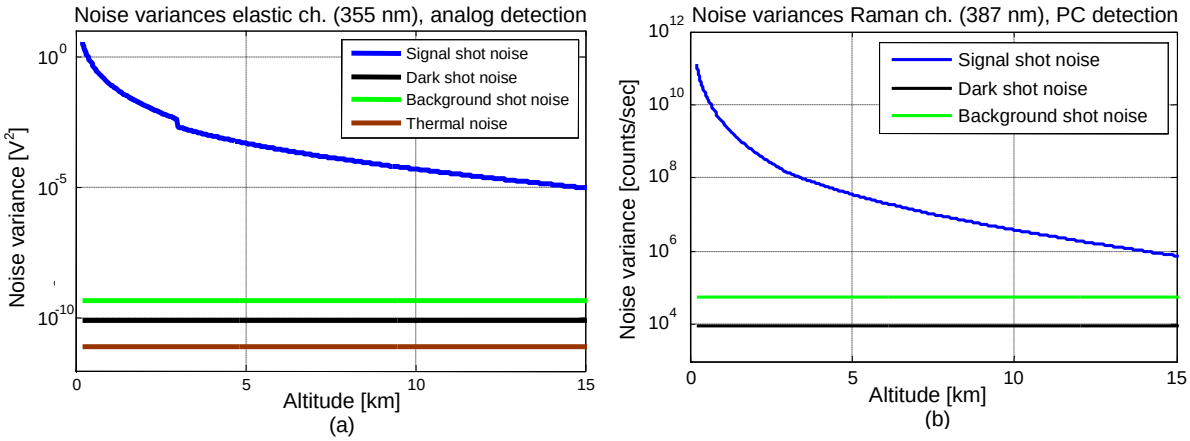

Figure 15. (a) Variances of signal shot noise, dark current shot noise and background noise versus range for the elastic channel. (b) Variances of signal shot noise, dark current shot noise and background shot noise versus altitude for the Raman channel.

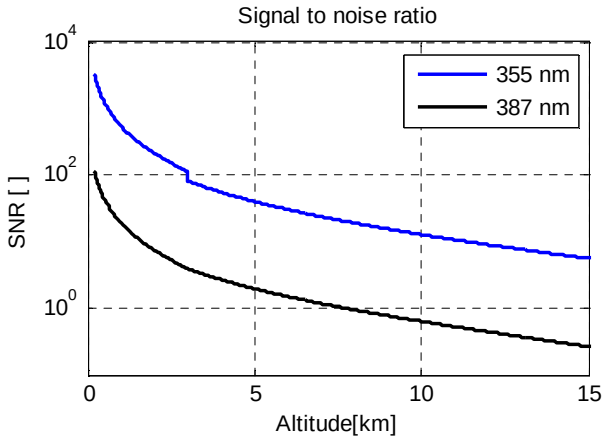

Figure 16. SNR for elastic (355nm) and Raman (387nm) Channel

SNR for a single pulse is plotted in Figure 16. Several pulses can be integrated to achieve a required SNR. In that case, the observation time has been calculated from (25) and is plotted in Figure 17 for the most restrictive case (SNR_{goal} = 10). Since the received power in the elastic channel is around 3 orders of magnitude higher than in the Raman channel, it is safe to say that the observation time for the whole system will be determined by the Raman channel restrictions, as it is showed in Figure 17.

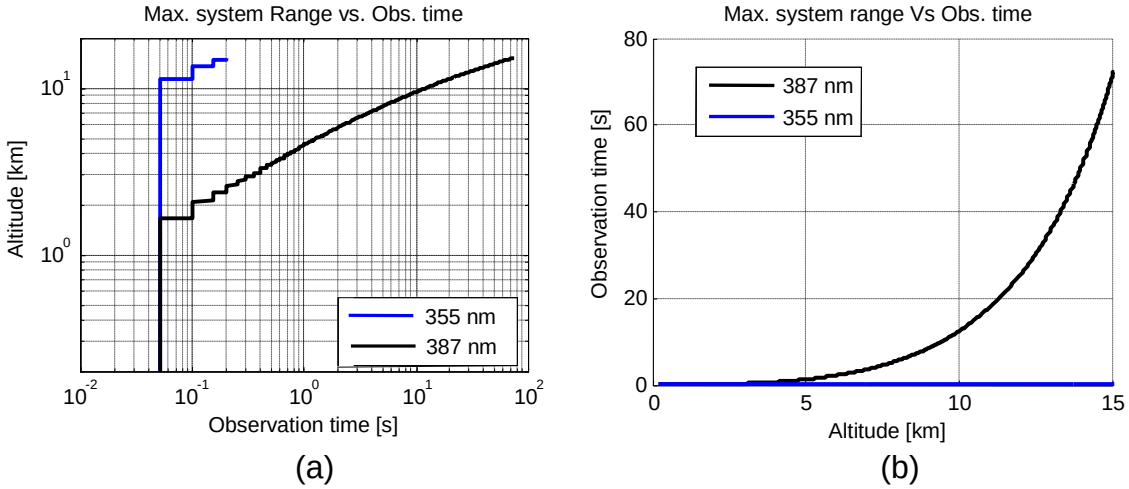

Figure 17. Observation time versus Range for a minimum required SNR of 10. (a) Plotted in logarithmic scale (b) Plotted in linear scale

About 77 seconds are needed to get data from up to a 15km high and 27.5 seconds to reach the typical altitude (12km) where the EAS take place. However, the time to take measurements up to a certain altitude increases when the lidar is not pointing vertically but with some angle θ respect to the zenith direction. The range increases with θ and also the number of aerosols and molecules that interact with the LASER beam (Figure 18a). That effect can be seen in Figure 18b for a constant height of 12km.

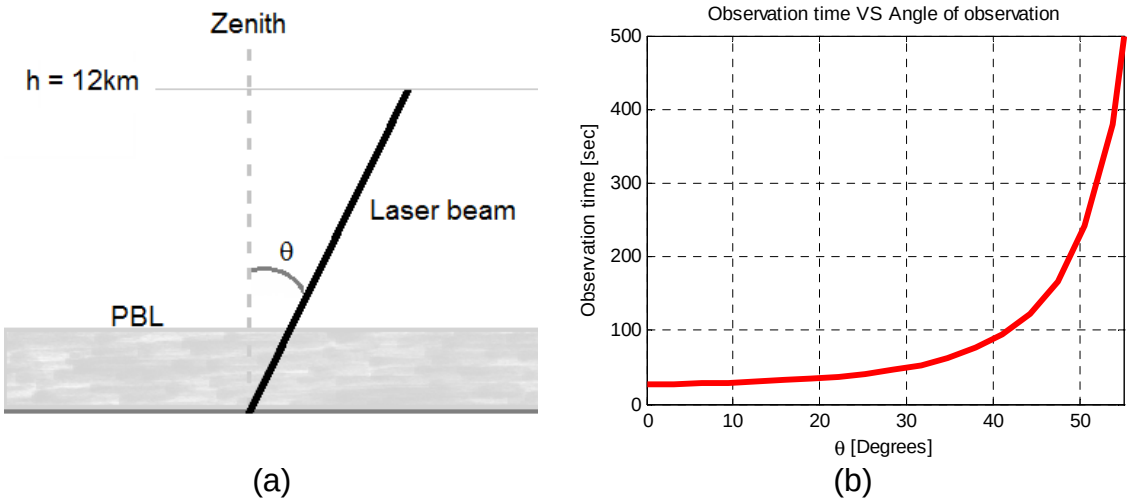

(a) (b)

Figure 18. Sketch of the laser beam pointing to a direction different form Zenith (a) and plot of the observation time versus the angle of observation respect to Zenith to reach a height of 12km (b)

By limiting the observation we can compute the maximum angle of observation. For instance, if our system averages pulses for 100 seconds, which is a typical time [11], atmosphere characterization will be possible within a radius of 16km.

Chapter 3. System details and parameterization of the observation time for different subsystem configurations

The LIDAR system must be optimized for the project needs by choosing the correct components. A brief description about the devices that compose IFAE-UAB LIDAR is detailed next, as well as the parameters that take an important role in the power link budget.

3.1. LASER

The LIDAR we will be using is equipped with a Nd:YAG laser from Brilliant. The fundamental wavelength of the laser is 1064 nm and third harmonic generation (THG) is used to produce light at a 355nm wavelength. Main parameters can be found in Table 1. It is the cheapest commercial solution for atmosphere characterization at the wavelength where EAS take place (peak energy at 330 nm). The laser also emit at 532 nm by second harmonic generation. This option could eventually be used to characterize the atmospheric transmission at both ends of EAS spectrum by adding two more channels to the LIDAR.

PRF (Hz)	10	20	50
Energy per pulse (mJ)	65/100	60/70	20

Table 2. Energy per pulse for different pulse repetition frequencies

For the same average power, higher pulse energy at a lower pulse repetition rate is preferred because SNR is improved in this way [11]. This laser can work with 3 Pulse Repetition Frequencies; 10Hz, 20Hz and 50Hz. The energy per pulse is different in all of them and for 10Hz and 20Hz an extra option to increase the energy is available (see Table 2). The lowest observation time (see Figure 19) is achieved by using a PRF equal to 20Hz. As the observation time in the standard mode (with 60mJ per pulse) and in the special mode (with 65mJ per pulse) are very similar, a low energy per pulse is preferred to extend the laser's life.

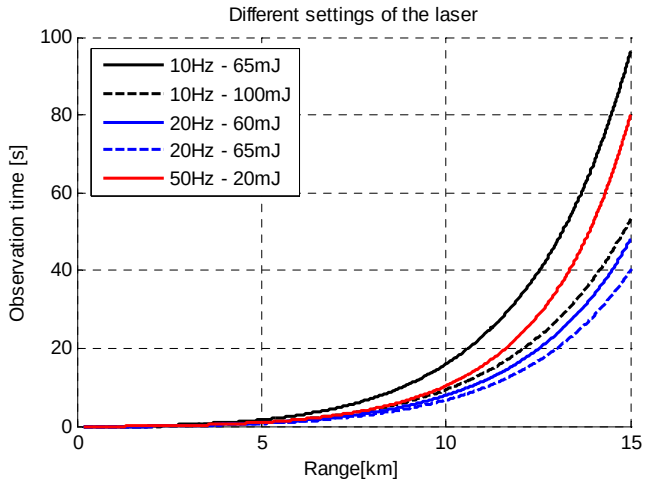

Figure 19. Observation time versus range for different laser settings (min. SNR of 10)

The laser beam is guided with two flat mirrors, as shown in Figure 9, to emit the beam coaxially to the telescope into the atmosphere. Its divergence is 4 times lower than the telescope field of view, thus there is no need for using beam expanders [11].

3.2. Telescope

The telescope is one of the set that CLUE project (1987-2002) had to measure Cherenkov light in La Palma and it will be reused for the IFAE-UAB LIDAR after some modification in the mechanics. The diameter of the parabolic mirror is 1.8 meters as well as its focal length. Its dimensions are quite large for a typical LIDAR system but, since the irradiance of the night sky in La Palma is very low compared to night sky in urban areas, it has been shown (see Figure 15) with the link budget simulations that the system is not dominated by the power collected from the background.

Figure 20. View of the telescope

The mirror transmissivity was measured in [20] and it is about 50-60%. Also the Point Spread Function was measured. Light arrive to the focal plane of the telescope with a Gaussian distribution in which the 90% of the light falls in a 4mm radio circle [21]. This high PSF is the main drawback of reusing this telescope because they condition the polychromator unit's optic design.

On a first approach, Background and dark current noise can be neglected from SNR in photon counting mode if the system is dominated by signal shot noise, as it is the case (see Figure 15). With this approximation

$$\mathrm{SNR_R} \approx \sqrt{\mathrm{P_{ram}}\xi_{\lambda_R}\mathrm{R_{io}}/\mathrm{q}}\,\sqrt{\tau} \qquad (27)$$

SNR increases by the square root of the telescope's area, or in other words, with its diameter. Therefore, every time that the telescope diameter is doubled,

the observation time is reduced approximately by 4. Figure 21 shows the exact simulated observation time varying the telescope diameter.

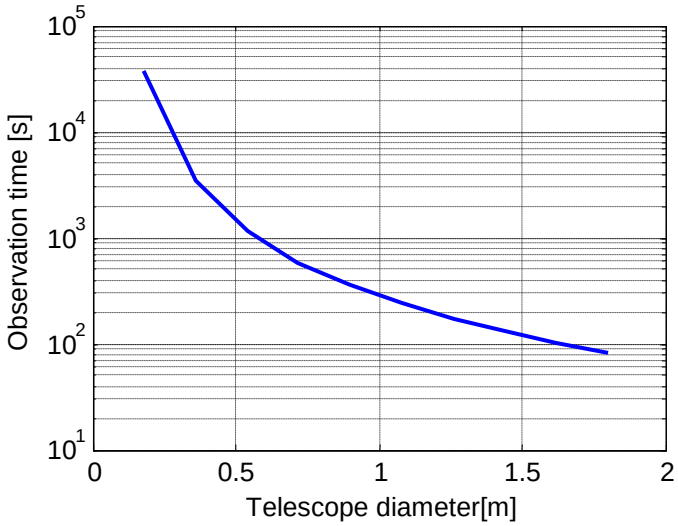

Figure 21. Observation time vs telescope diameter (SNR_{goal} = 10)

It is possible that in a near future the mirror is coated again improving its reflectivity from 55% to 95%. This will translate into a reduction of the observation time from 77s to 47s at a range of 15km and for a required SNR of 10. This coating work is also convenient since the observation time grows rapidly for a mirror reflectivity lower than 0.4 as it is shown in Figure 22. In the current status of the mirror, the telescope has an effective diameter of 1.27m, despites of its actual diameter of 1.8m.

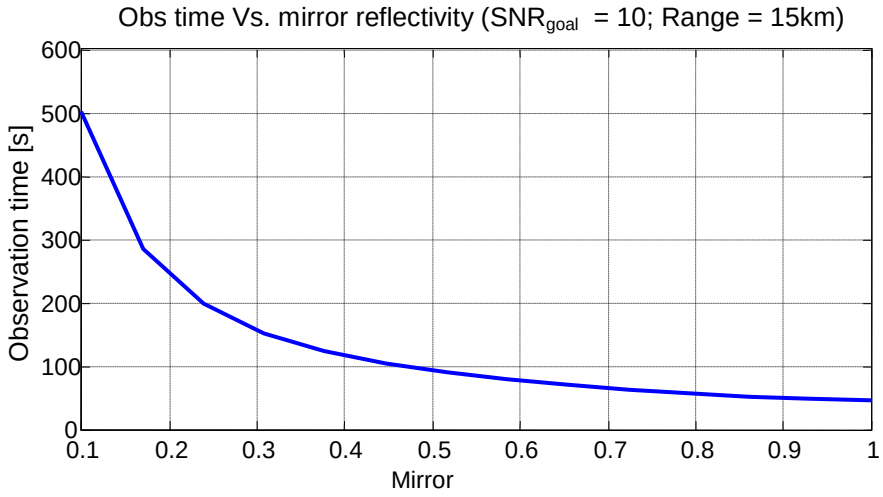

Figure 22. Observation time for different mirror reflectivities

3.3. Liquid light guide

A light guide is used to convey the light from the telescope focal plane to the polychromator unit. As the telescope concentrates rays in an 8mm circle, a liquid light guide of the same section was chosen. It is the Lumatec s300 and it is designed to work with these wavelengths of interest in the UV, showing a transmission of 75%.

The numerical aperture was measured in the IFAE laboratory. This measurement shows the dependency between the angle of incident light and the outgoing light angle. The light condensed by the telescope enters into the fiber with a maximum angle of arctang (1.8/0.9) = 26.57º deg. For this angle of aperture of the liquid guide results to be 34º (half angle).

3.4. Polychromator unit

In the polychromator unit, the light is distributed from the light guide to the different sensors. For such purpose, a set of lenses, a dichroic mirror, and interference filters are used. Initially, the box is composed by two sensors but it has been designed to eventually accept more channels with the minimum changes possible. A description of the proposal design for the polychromator unit can be found in Chapter 4.

3.5. Photomultiplier tubes

The most commonly used sensors for the UV frequencies are Photomultiplier Tubes (PMT's). As explained in section 2.2.4, they are composed by a photocathode, a set of dynodes and an anode. For every photon that reaches the photocathode η electrons are emitted and multiplied by secondary electron emissions through the dynodes, being η the PMT quantum efficiency. Between all the possible PMT in the market a Bialkali PMT of Hamamatsu has been chosen because they have higher quantum efficiency at the UV wavelengths than other sensors. The R1924A PMT shows its quantum efficiency peak (25%) at wavelengths of 350-400nm.

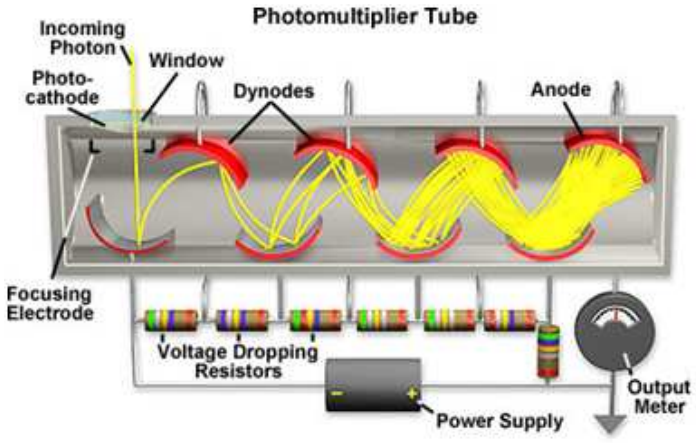

Figure 23. Section sketch of a PMT [22]

There exist a range of PMTs of different diameters for UV wavelengths. It is advisable to choose the smallest one possible to reduce the anode dark current. Nevertheless, the design of the polychromator unit is not straightforward since the aperture and section of our light guide are quite larger than desirable. Even if it is possible to use PMTs of 8mm for the two first channels, the following PMTs must be larger (See chapter 4).Therefore, we could then say that it is

preferable that all of them PMTs are from the same kind to make a hypothetical future replacement faster, easier and more efficient. Additionally, simulations with a larger one have been made. Their parameters are summarized in Table 3.

PMT model	R7400U	R1924A
Equivalent active area diameter [mm]	8	22
Multiplication factor [ ]	7e5	2e6
Anode dark current [nA]	0.2	3
Anode radiant sensitivity [mA/W]	60	55

Table 3. R7400U and R1924A parameters

For both PMTs, the system is dominated by the signal shot noise as shown in Figure 24 (a) and Figure 24 (b). Signal shot noise variances in the elastic and Raman channel are above other noise variances. Even if the anode dark current is 15 times higher in the 22mm PMT, the changes in SNR are not appreciable; not even in the observation times Figure 25.

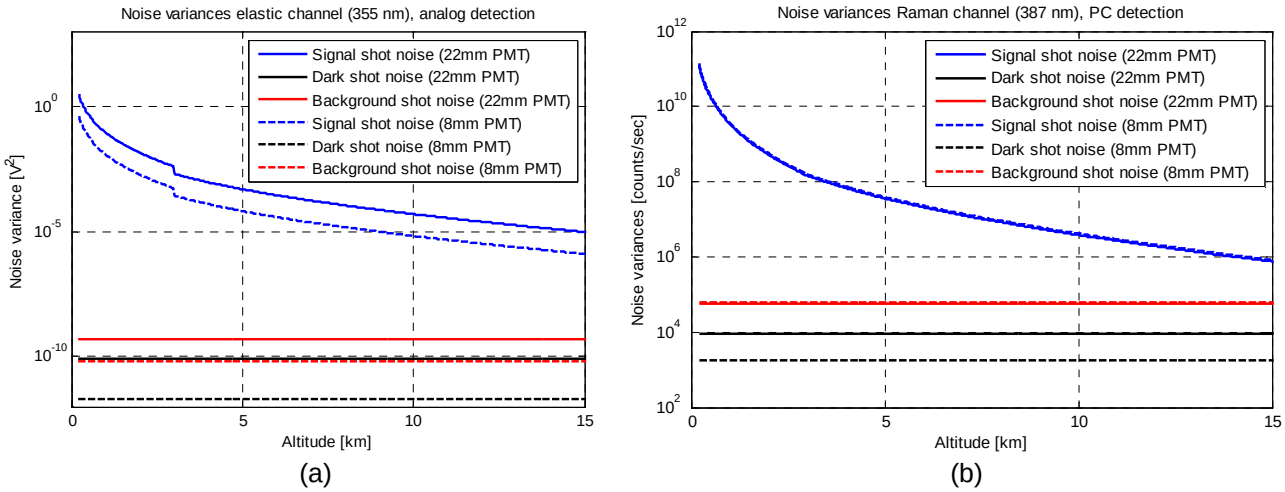

Figure 24. Comparison between a 22mm and an 8mm diameter PMTs. (a) Noise variances versus range for the elastic channel (b) Noise variances for the Raman channel.

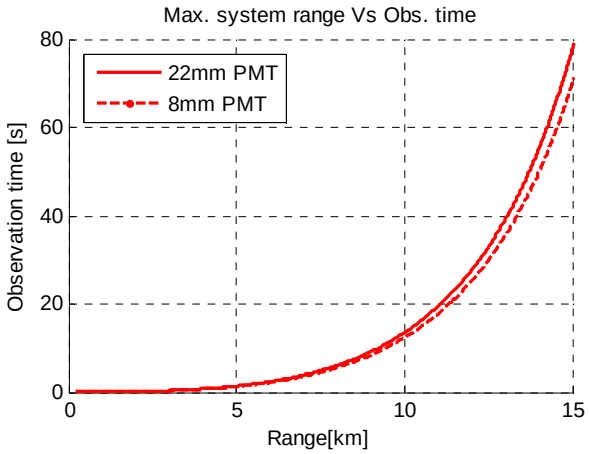

Figure 25. Observation time versus range for two different PMTs.

To avoid over passing the maximum current of the photocathode a gated PMT solution (i.e., including an electronic enable/disable feature) will be used to disable reception during the first 200 m of the LIDAR signal where, due to the laser-telescope coaxial arrangement, the detectors become blinded. For the elastic channel, it is envisaged inclusion of neutral density filters to accommodate the return power levels to levels comparable to those of the Raman channel, since with such a large-aperture telescope, the input light levels can drive the PMT detector deep into saturation.

3.6. Transient recorder

The output current from the PMTs is acquired by a transient recorder LICEL TR20-160. The signal is recorded simultaneously by an Analog to Digital Converter (ADC) of 12 Bits at a sampling rate of 20 MSamples/sec and a discriminator which detects voltage pulses above a selected threshold (See Figure 26).

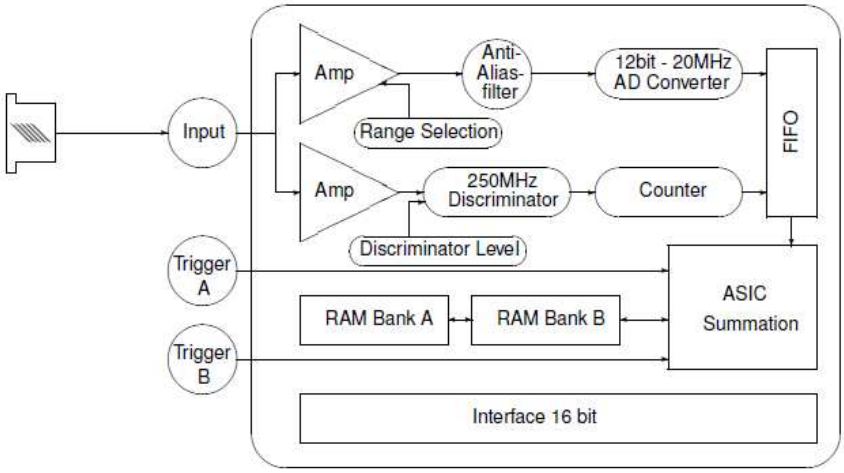

Figure 26. Schematic setup of the LIDAR trancient receiver TR20-160 [23]

For analog detection the signal is amplified, according to the input range selected, and signals below a frequency of 10MHz are passing the anti-alias filter to be digitized by a 12 bit ADC. Each signal is written to a fast memory which is readout after each shot and added to the summed signal in a RAM. Depending on the trigger input on Trigger A or trigger B the signal is added to ram A or B, which allow acquisitions of to repetitive channels if these signals can be measured sequentially.

At the same time the signal part in the high frequency domain above 10MHz is amplified and a 250 MHz discriminator detects single photon events above the selected threshold voltage. Two different settings of the preamplifier can be controlled by software together with 64 different discriminator levels. Again the signal is written to a faster memory RAM after each acquisition cycle.

An acquisition system using the TR20-160 can be configured for up to 16 simultaneous detection channels. Such a system is configured by using a HF cassette mounted transient recorder module for each channel, a rack comprising power supplies and an interface ports and a computer which.

Chapter 4. The polychromator unit

The beam light collected by the telescope contains the inelastic and elastic channels. It travels through the light guide to be filtered and detected afterwards. In an intermediate step, the different parts of the spectrum must be isolated and redirected to the correspondent sensor. This is made inside the polychromator unit, which is a box equipped with filters, lenses and mirrors to direct the light towards the PMTs.

The design of the polychromator unit is critical in order to evaluate the net optical losses of the LIDAR. During this chapter, a first attempt for the polychromator unit is proposed, which aims not at describing the final components of the unit but to evaluate the necessary elements, their size and the losses of the optical paths.

A first study with paraxial calculations can be formulated to determine critical parameters such as focal lengths, diameter and position of images and objects. Nowadays, any optical design cannot be conceived without the use of ray tracing simulation software. ZEMAX^{TM} is a tool for optical engineers to design, analyze and optimize any optical system [24]. The use of this tool has helped to describe the appearance of the polychromator unit in terms of size and position of the elements used.

4.1. ZEMAX^{TM} ray-tracing simulation

Here a proposal for the polychromator unit of the IFAE-UAB Raman Lidar is presented. The proposed design for a two channel polychromator unit fits in a 26cm x15cm. Its framework has an inverted 'T' shape, receiving the light from the left side port and detecting elastic and inelastic channels from the top and right ports. It was designed with the intention of developing a modular unit, with the possibility of adding more channels with minimum changes. Therefore, one output port would be at the right side and the rest at the top.

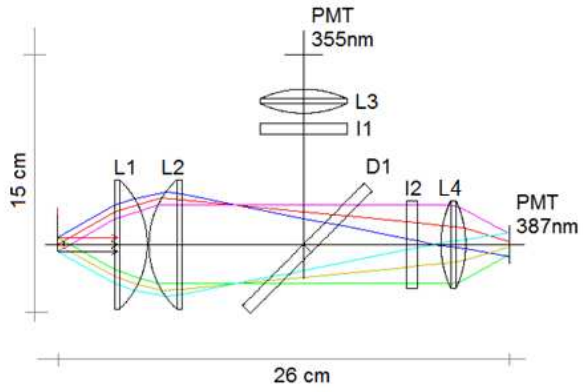

Figure 27. Polychromator design layout and related ZEMAX^{TM} ray tracing at 387 nm (elastic channel) and 387 nm (nitrogen Raman channel). (D1) Dichroic mirror; (L1, L2, L3, L4) Lenses; (I1, I2) Interference Filters.

Figure 27 shows the ray tracing simulation of the two channel polychromator unit. The light outing of the liquid light guide is condensed with two plano-convex lenses L1 and L2 and then the signal is split for the elastic and inelastic channels by a Dichroic Mirror D1. Afterwards, the interference filter I1 filters the signal centered in the elastic Central WaveLength (CWL) and a bi-convex lens L3 focus the beam on the PMT photo-cathode. Analogously, the interference I2 and the lens L4 perform the same function with the inelastic channel.

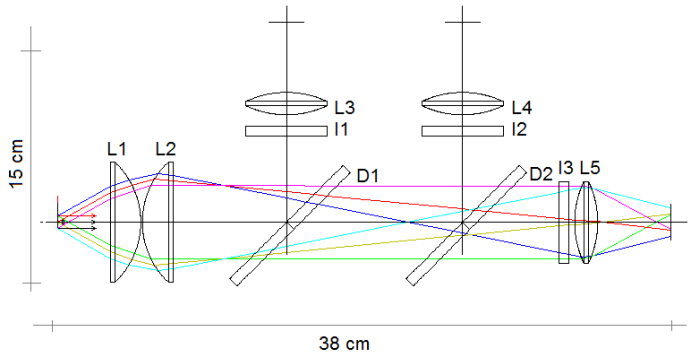

Figure 28. Polychromator design layout and related ZEMAX™ ray tracing for a 3 channel polychromator unit (Labels of this sketch do not match with the Table 4)

The divergence of the light guide and its diameter has conditioned the size of the optic elements. L1 and L2 lenses have a diameter of 75 mm, the largest plano-convex lenses that THORLABS manufactures. They condense the light in a beam smaller than the diameter of the plano-convex lenses used (50.8 mm). The distance that the light travels in such condition is long enough to admit the inclusion of an additional channel. Figure 28 shows the sketch of the three channel polychromator unit. The lenses remain but the interference filter and the dichroic mirror must be reconsidered. In case a forth channel wants to be considered, the proposed configuration cannot condense the light sufficiently and therefore either an additional condensation step is needed or a reformulation of the whole optical system. The specification for the two channels unit can be found Table 4 and a brief description of each device is given in the next section.

Dichroic mirror	1.5" DIA x 0.2 "T		
Size	ρ ≥ 90% @ 355nm		
*ρ, τ	τ ≥ 90% @ 387 nm		
Lenses	DIA (mm)	Effective Focal Length (mm)	Model (THORLABS)
Plano convex Lens (L1, L2)	75	38.0	LA1238
Bi convex Lens (L3,L4)	50.8	60	LB1723
Interference Filters (I1, I2)			
CWL (nm.)	355 ± 1.5	387± 1.5	
FWHM (nm.)	10 ± 2.0	10 ± 2.0	
% τ	Peak > 60%	Peak > 65%	
Out of band blocking	>OD 5 200-1100nm	>OD 5 200-1100nm	

Table 4. Polychromator specs of the 1+1 channel elastic/Raman polychromator. ρ and τ respectively represent reflectivity and transmissivity. Also, DIA stands for diameter. All lenses transmission is 90%.

4.2. Description of the polychromator unit components

Here a short description of each component in the polychromator unit is given: the light guide, the condenser lenses, the dichroic mirror, the interference filters and the eye-piece.

Liquid light guide model

The whole optical design is constrained by the light guide diameter and divergence (See section 3.3 for a description of the liquid light guide). As the telescope concentrates the light in an 8mm spot (with a loss of 10%) the liquid light guide used has that same size. Measurements over the light guide show that the light comes out of it with an aperture of 34º (half angle). One end receives the light from the telescope while the other one is connected to the polychromator unit, illuminating the designed paths inside it. This end can be seen as an infinite set of point sources distributed over its circular section. In order to simulate the light coming out from the light guide, we have modeled its section as 3 point sources, vertically placed and separated 4mm with the same aperture as the light guide.

The main objective is to emulate the light coming out of the light beam with its 34º angle. This can be seen in the figure below:

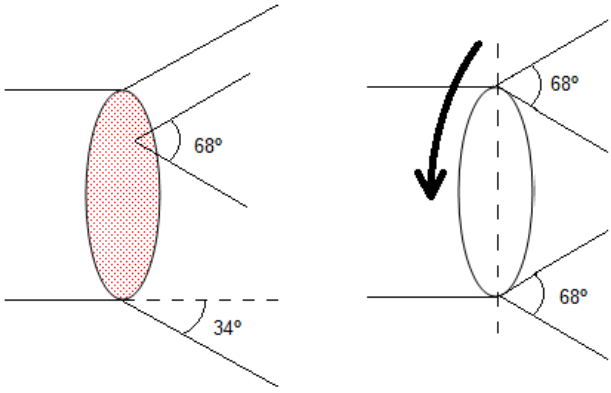

Figure 29. Modeling of the light guide end as an infinite set of point sources (left) and simulated model with two exterior point sources where rotational geometry can be applied.

The Figure 29 can be inferred as the transversal section of the beam light and rotational geometry can therefore be applied. By doing so, all possible rays coming out from the light guide are covered.

Condenser lens

The end of the fiber cannot be considered as a point source which is an important inconvenient. A point source can be collimated with a plano-convex lens by placing it at its focal distance F (Figure 30). However, the lens is not

design for collimating the light that comes from the focal plan with a certain height. As a result of the former, the rays coming out of lens are not parallel, so that they diverge. Also, the large aperture of the fiber requires large lenses placed very near to avoid the light overflow.

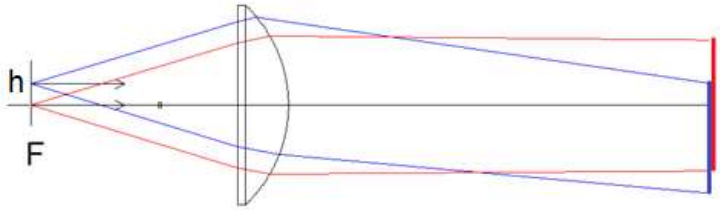

Figure 30. Simulation of rays coming from a point source at the focus of a plano-convex lens (red rays) and rays coming from the focal plane of the lens with a certain height (blue rays).

A condenser configuration with two plano-convex lenses has been used to reduce the divergence of the beam light. It makes use of the larger lenses that Thorlabs manufactures. This configuration allows enlarging the optical paths enabling the addition of more channels (Figure 31), however by using two lenses instead of one, the transmissivity decreases from 0.9 to 0.8.

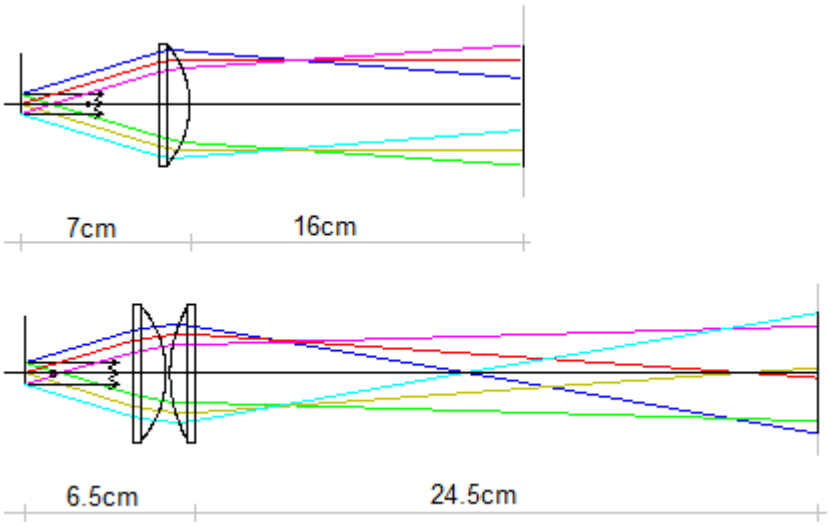

Figure 31. Ray tracing simulation for three point sources placed at the focal plane of a plano-convex lens (above) and ray tracing simulation for three point sources illuminating two plano-convex lenses in a condenser configuration. The rays are drown up to their aperture is the same as the diameter of the eye-piece used.

Dichroic mirror

Elastically backscattered light in the Raman channel must be suppressed because it is around 3 orders of magnitude higher than the light in the Raman channel. In the polychromator unit, the beam light must be split in frequency and space domains in order for the beam to be detected by the PMTs: This is the task of the dichroic mirrors, tilted 45º degrees to the direction of the light propagation. These mirrors reflect the part of the spectrum below the designed wavelength upwards; and transmit forward the part of the spectrum above this wavelength (Figure 32). For instance, dichroic mirrors are used in LCD projectors to extract the red, green, and blue light from the white light and project color composed images.

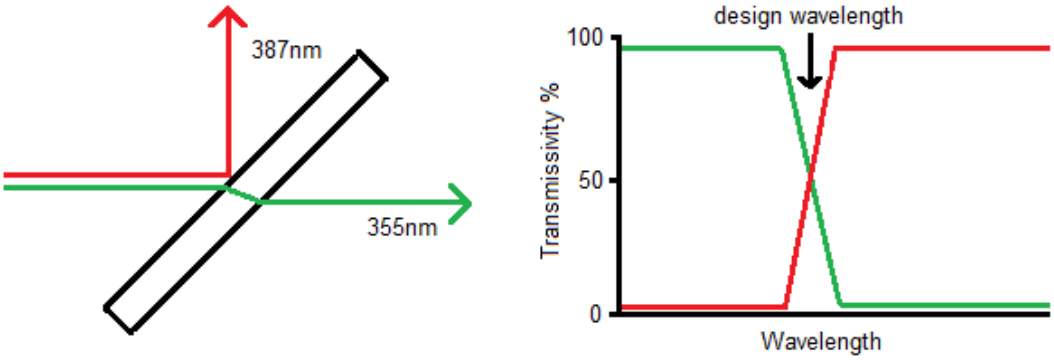

Figure 32. Sketch of the ray tracing in a dichroic mirror (left) and its transmisivity depending on the wavelength (right).

Dichroic mirrors are commonly used in visible spectrum and they are easy to find in optic manufacture's catalogs. However, dichroic mirrors for UV wavelengths are usually manufactured by request. The manufacturer Materion is currently producing the dichroic mirror for the IFAE-UAB Raman LIDAR which transmissivity and reflectivity are larger than 90% at 387nm and 355nm respectively. This transmissivity and reflectivity have to be measured because the mirror design wavelength changes when the light incidence angle is different than 45º [25].

Interference filters

Interference filters are needed to reduce the noise and therefore increase the Signal-to-Noise Ratio. Usually, the narrower the filter is the better the SNR. On the other hand, and as we have seen throughout this paper, the received power from the background is proportional to the interference filter bandwidth but it is not determinant in the observation time nor in the SNR.

The Central WaveLength (CWL) of the interference filter is sensitive to the light incidence angle, like in the dichroic mirrors. Since this effect has not been yet evaluated, we have decided to use the safest option and we have therefore chosen a 10 nm bandwidth filter (FWHM: Full-Width at Half-Maximum). Figure 33, shows that the performance of the Raman LIDAR does not significantly change when having a 10 nm or a 1 nm filter, since as stated in previous sections the system is dominated not by the background shot noise but by the signal shot noise.

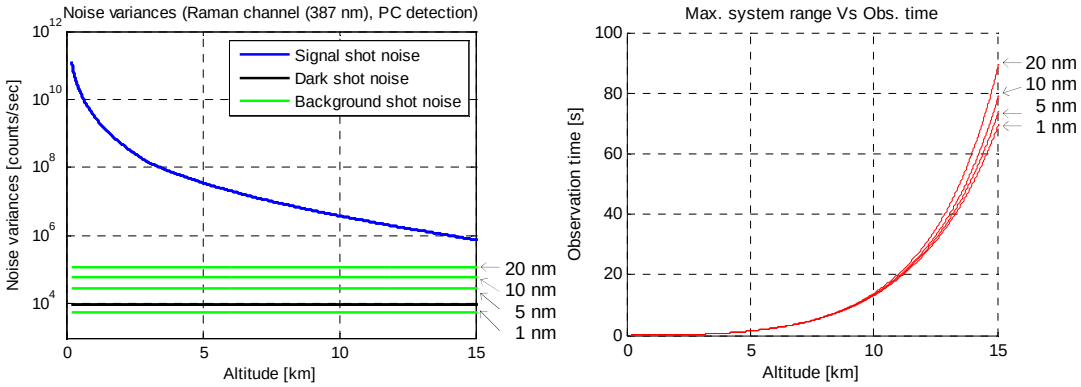

(a) (b)

Figure 33. Evaluation of the LIDAR for diferent interferent filter bandwidth. Noise variances (a), Observation time Vs. Range (b)

The transmissivity of each filter is 0.60 and 0.65 in the elastic and inelastic channels respectively. Out of the transmission band, both filters present an Optical Density (OD) of 5, or in other words, a transmissivity of 10^{-5} out of the band.

Eye-pieces

Eye-pieces are the last step in the optical path. Their function is to focus the light onto the photocathode of the PMT while covering its entire surface. We have used the largest bi-convex lenses manufactured by THORLABS. Since the beam light diverges, the diameter of the lenses limits the path length and the number of channels that the polychromator unit can contain.

Chapter 5. Conclusions

The concept design of the IFAE-UAB Raman LIDAR has been presented in this master thesis. The design is the outcome of the analysis of the LIDAR theory done to identify which key parameters change the performance of the system significantly. To do so, we have relied on computing the power link budget, the SNR in the reception channel and finally the estimated observation time needed.

First, it has been shown that the IFAE-UAB Raman LIDAR fulfils the requirements in terms of observation time. Therefore, the atmosphere can be characterized by means of such LIDAR between two consecutives measurements of the IACT while they change their pointing position.

Second, it has been also inferred from the power link budget analysis that the Raman LIDAR is dominated by signal shot noise, due to the large telescope area and the low irradiance of the night sky in La Palma. Particularly, background received power is much smaller when comparing with LIDAR returned signal. Therefore the differences in the observation time when using narrower or wider interference filter bandwidths is negligible.

Third, it has been shown that small differences in the performances of our LIDAR are observed when we use a PMT of a smaller detection area, which is generally preferred. This is because the dark shot noise of the PMTs is much below than the signal shot-noise level.

Fourth, the large point spread function of the telescope makes it difficult to guide and concentrate the light onto the sensors and forces to use large PMT detection areas. Furthermore, it has been shown that the worn out mirror reflectivity is critical in the performance of the LIDAR and it is recommended to change or recoat the mirror to improve the effective area of the telescope.

Finally, we can conclude that the results presented here concerning the observation are conservative enough since a relatively high value for the minimum SNR required by the inversion algorithm (SNR_{goal}) have been used. This algorithm will be developed in future stages.

Besides from these main conclusions, a proposal for the polychromator unit has been presented (chapter 4). This design admits the eventual addition of another channel by just replacing the dichroic mirror. The model is presented here is just a preliminary design to evaluate the optical losses in the polychromator unit. However, further refinements are needed in order to achieve optimal specifications.

References

[1] Tescaro, D. "TeV gamma-ray observation of nearby Active Galactic Nuclei with the MAGIC telescope: exploring the high energy region of the multiwavelength picture." IFAE-UAB, Barcelona, 2010.

[2] Hofmann, J.A. Hinton and W. "Teraelectronvolt Astronomy." *ARA&A* 47 (2009): 523-565.

[3] Hrupec, Dario. "Extragalactic sources of rapidly variable high energy gamma radiation (Doctoral Thesis)." Department of Physics, Faculty of Science, University of Zagreb, Zagreb, 2008, 61-92.

[4] Agency, U.S. Environmental Protection. *Planetary Boundary Layer Modeling for Meteorology and Air Quality.* 2010. http://www.epa.gov/AMD/ModelDevelopment/landSurfacePBL.html.

[5] J. Zarauz, A. Ghula, R. Pasken. "SULFUR DIOXIDE ESTIMATIONS IN THE PLANETARY BOUNDARY LAYER USING OZONE MONITORING INSTRUMENT." 2010.

[6] Garrido, D. "The effect of molecular and aerosol atmospheric profiles on the performance of the MAGIC telescopes." IFAE-UAB, Barcelona, 2011.

[7] Smullin, L. D. and Fiocco, G. "Optical echoes from the moon." *Nature* 194 (1962): 1267- 1267.

[8] F. Rocadenbosch, I. Mattis and others. "The European Aerosol Research Lidar Network (EARLINET): An Overview." *IEEE International Geoscience and Remote Sensing Symposium (IGARSS)* 2 (2008): II-410 – II-413.

[9] Limited, Bluesky International. *LiDAR UK.* http://www.lidar-uk.com/.

[10] al., A. Behrendt et. "Combined Raman Lidar for the Measurement of Atmospheric Temperature, Water Vapor, Particle Extinction Coefficient, and Particle Backscatter Coefficient." *Appl. Opt.* 41, no. 26 (2002º): 7657-7666.

[11] (Ed.), Claus Weitkamp. *LIDAR : range-resolved optical remote sensing of the atmosphere.* Springer, 2005.

[12] Inaba, H. *Detection of Atoms and Molecules by raman Scattering and Resonance Fluorescense.* Vol. 14, in *Laser Monitoring of the atmosphere*, edited by E. D. Hinkley, 153-237. 1976.

[13] Koshmieder, H. "Theorie der Horizontalen Sichtweite." Beitr. Phys. Freien Atmos., 1924.

[14] Russel, R.T.H. Collis and P.B. *Laser Monitoring of the Atmosphere (CH 4. Lidar measurements of Particles and Gases).* Edited by E. D. Hinkley. 18 vols. Berlin Heidelberg New York: Springer, 1976.

[15] Galvez, M.C.D. and Alarcon, M.C. and Kobayashi, T. "Angstrom Coefficient of Tropospheric Cloud and Aerosol Derived From A Three-Wavelength Mie Lidar System." *Lasers and Electro-Optics* 3 (1999): 939 - 940.

[16] B. A. Bodhaine, N. B. Wood, E. G. Dutton, J. R. Slusser. "On Rayleigh Optical Depth Calculations." *Journal of Atmospherice and Oceanic Technology* 16, no. 11 (1999): 1854-1861.

[17] (AMS), American Meteorological Society. *Glosary of Meteorology.* 2000.

http://amsglossary.allenpress.com/glossary/search?id=standard-atmosphere1.

[18] Mirzoyan, R. "Cherenkov light observation with the HEGRA detector at the Roque de los Muchachos Observatory." *New Astronomy Reviews* 42 (1998): 547–551 .

[19] Photonics, Hamamatsu. *PHOTOMULTIPLIERS TUBES, Bases and Applications.* 3rd. Word Technical Writing, 2007.

[20] López, A. "Construction and Development of a Raman Lidar." Universitat Autònoma de Barcelona, 2010.

[21] Alonso, Carlos Sánchez. "Caracterització del LIDAR de CTA." Departament de Física, UAB, Barcelona, 2011.

[22] Photnonics, Hamamatsu. http://learn.hamamatsu.com/articles/photomultipliers.html.

[23] Licel. "Lidar transient recorder. Manual." Berlin, 2010.

[24] ZEMAX. "Getting Started Using ZEMAX."

[25] Optics, Edmun. *Edmun Optics, Technical support, Optical filters.* 2011. http://www.edmundoptics.com/technical-support/optics/optical-filters/?&viewall.

[26] A. Ansmann, U. Wandinger, M. Riebesell, C. Weitkamp, W. Michaelis. "Independent measurement of extinction and backscatter profiles in cirrus clouds by using a combined Raman elastic-backscatter lidar." *Appl. Opt.* 31(33), no. ISSN 0003-6935 (1992): 7113-7131.

ANNEX

ARTICLE TO BE SUBMITED TO: Monthly Notices Royal Astron. Soc., (MNRAS), IF=5.185 (2008).

Concept design of an elastic/Raman Lidar for atmospheric characterisation in Cherenkov-telescope astrophysical studies

Dhiraj Kumar[a], Francesc Rocadenbosch[a], Miguel Eizmendi[a,b], Michele Doro[b], Lluís Font[b], Oscar Blanch[c], Alicia López-Oramas[c], Manel Martínez[c]

[a]Universitat Politècnica de Catalunya (UPC), Dept. of Signal Theory and Communications (TSC), Remote Sensing Lab (RSLab), E-08034 Barcelona, Spain/Institute of Space Studies of Catalonia (IEEC-CRAE).

[b]Universitat Autónoma de Barcelona (UAB), Dept. of Physics, E-08193 Bellaterra, Spain.

[c]Institut de Física d'Altes Energías (IFAE), E-08193 Barcelona, Spain

ABSTRACT

Ground-based Cherenkov telescopes of the Imaging Atmospheric Cherenkov Telescope (IACT) class detect cosmic gamma-rays above few tens of Giga-electron-Volts, by observing the Cherenkov light produced in Extensive Atmospheric Showers (EAS) initiated by the interaction of the primary cosmic gamma-ray with the atmospheric constituents. The current generation of IACTs, and specially HESS, MAGIC and VERITAS, has most of their systematic errors in the energy reconstruction and absolute scale of the gamma-ray measured fluxes due to uncertainties in the determination of the opto-atmospheric parameters.

This work reports on the current design of a tropospheric elastic/Raman lidar (355/387-nm wavelength) system to be used for determination of the sought-after atmospheric parameters of interest (namely, extinction and backscatter). Concept-design of the IFAE/UAB lidar system including system architecture and specs, opto-atmospheric parameter modelling, formulation of the power link-budget, and assessment of the system performance [signal-to-noise ratio (SNR), and maximum system range as a function of

observation time] is presented. The lidar will be installed and operated at the Cherenkov Telescope Array (CTA) observatory, which is the future generation of IACTs.

KEYWORDS

Lidar, backscatter, Raman, atmospheric calibration, Cherenkov telescopes, Astrophysics, MAGIC, CTA.

1. INTRODUCTION

Ground-based Cherenkov telescopes of the Imaging Atmospheric Cherenkov Telescope (IACT) [25] class observe cosmic gamma-rays in the GeV–TeV regime[1] by collecting the Cherenkov light [27] produced by electrons and positrons in electromagnetic showers initiated by primary cosmic gamma-rays when interacting in the top Earth atmosphere. When a primary gamma-ray reaches the atmosphere a pair electron-positron is produced. The charged particles re-emit secondary gamma-rays via Bremmstrahlung. The secondary gamma-rays, in turn, pair-produce electrons and positrons, and so on. Therefore, a shower of hundreds of particles is developed along several tens or hundreds of meters. The energy of the electrons in each step of the shower is roughly half of that of the previous step until it reaches the ionization yield and the shower dies [26].

In the first stages of the showers, the electrons travel at a speed greater than the speed of light in the atmosphere and, therefore, produce Cherenkov light. This light is a ultraviolet (UV)-optical flash of the duration of few nanoseconds, in the shape of a cone aligned with the primary gamma-ray direction, which illuminate the ground in a circle of roughly 120 m radius after having crossed the atmosphere. Whenever an IACT is placed inside the Cherenkov light pool and given that enough Cherenkov photons hit the mirror, the shower is recorded and through an image reconstruction, the energy, direction, and arrival time of the primary gamma-ray are obtained [28].

The current generation of IACTs, and specially HESS, MAGIC and VERITAS [22] (Fig. 1) has most of the systematic errors in the energy reconstruction and absolute scale of the gamma-ray measured fluxes due to systematic errors in the determination of atmospheric parameters. Of particular concern is the poorly known total extinction that Cherenkov photons undergo in their travel from the emission region, typically located between 20 and 10 km a.s.l., to the ground. Despite the fact that some instruments are currently used to measure the atmospheric transparency, their data are only used to retain good-quality observation time slots, and currently only a minor effort is done to correct data with atmospheric information [29][30].

On the other hand, the entire IACT community is now focussed on the design of a new generation of Cherenkov telescopes with improved performance. The leading project is the Cherenkov Telescope Array (CTA) observatory [23][31] (see Fig. 2), which is a worldwide effort for the construction of several tens of IACTs to be operated simultaneously, compared to the current generation of installations which comprises 2-4 telescopes. CTA will be operated by a wide international community of scientists and will be based on a high-quality level of data dissemination, which is typical for the larger astronomical installations. To reach this goal, the atmosphere should be monitored continuously and precisely, so that the data can be corrected offline before dissemination.

[1] 1 GeV = 10^9 eV, 1 TeV = 10^{12} eV (eV= electronvolt)

A precise monitoring of the atmosphere requires the use of remote-sensing sensors like the Raman lidars, which is the subject of this paper. Lidar (Light Detection and Ranging) has already been proved as a powerful tool in environmental studies since light directly interacts with the atmospheric constituents and thus provides the footprint of atmospheric species in return. The characterization of atmosphere can be successfully done at night using an elastic/Raman lidar system [1][2][3] which could be a good technique for data calibration in the energy reconstruction and absolute scale of the gamma-ray measured fluxes due to systematic errors in the determination of atmospheric parameters in the area of Astronomy [24].

With this aim, the Institut de Física d'Altes Energies (IFAE) and the Universitat Autónoma de Barcelona (UAB), in the context of the Atmospheric Calibration (ATAC) working group of CTA, and both members of the MAGIC collaboration, are currently designing a non-scanning pulsed elastic/Raman lidar system to be used for systematic data error correction due to poorly known molecular and particle extinction coefficients. The lidar will be installed and operated at the CTA site, currently under definition, with the goal of reducing the systematic uncertainties of the imaging atmospheric Cherenkov technique of the telescope and increasing the duty cycle thanks to a better knowledge of the atmosphere. Two other groups are also developing Raman lidars for CTA: the LUPM (Laboratoire Univers et Particules de Montpellier) in Montpellier (France) and the CEILAP (Centro de Investigaciones Láser y sus Aplicaciones) group in Villa Martelli (Argentina).

Non-scanning pulsed backscatter lidars (or elastic lidars) are the simplest class of lidar systems in which the emission of a laser pulse along a fixed line of sight is followed by reception, at the same wavelength, of the "optical echo" due to the intervening atmospheric constituents (molecules and aerosols). Because the elastic-backscattered power return (i.e., the measurement data) depends on two unknowns, the total optical atmospheric extinction and backscatter parameters (Sect. 3.2), it is not possible to invert them unless "a priori" correlation hypothesis and/or boundary calibrations are introduced [10].

Conceptually, a way out to come up with two measurement sets and two unknowns is the combination of one elastic and one Raman channel (*1+1* elastic/Raman lidar configuration), which enables independent simultaneous inversion of the optical atmospheric extinction and backscatter parameters [2][11]. In such an elastic/Raman lidar system, a two-channel receiver is used to "listen" to both the elastic-backscattered atmospheric radiation (i.e., with no wavelength shift) and to the inelastic-backscattered radiation (i.e., Raman shifted) due to any abundant atmospheric species (usually the nitrogen). The amount of wavelength shift is specific of the intervening species and is computed for the Q-branch of the vibrational Raman return spectrum [3]. The elastic/Raman lidar solution for atmospheric characterization is a mature solution within, for example, the European Aerosol Research LIdar Network (EARLINET) [13] -of which

the Remote Sensing Lab. (RSLab) of the UPC is member- and the GAW (Global Atmospheric Watch) Aerosol LIdar Observation Network (GALION) [16] worldwide. Other solutions based on HSRL (High Spectral Resolution Lidar) are also possible.

This paper is organized as follows: Sect. 2 presents an overview of the IFAE/UAB elastic/Raman lidar system, Sect. 3 focus on the atmospheric modelling of the optical parameters and assessment of the system performance (return power levels, range-dependent SNR, and maximum system range). The structure of the paper follows a previous UPC work in the design of its EARLINET multi-spectral elastic/Raman lidar system [17]. Finally, Sect. 4 gives conclusion remarks.

2. OVERVIEW OF THE IFAE/UAB ELASTIC-RAMAN LIDAR SYSTEM

The 1+1 configuration is the basis of the IFAE/UAB elastic-Raman lidar. A sketch of the system architecture is illustrated in Fig. 3a. System specs are given in Tab 1. The elastic channel operates at 355-nm wavelength (ultraviolet, UV) and the Raman channel at 387-nm wavelength (nitrogen Raman shift for a 355-nm excitation wavelength). In addition to the fact that Cherenkov radiation occurs mainly in the UV, a UV wavelength is chosen because of the higher atmospheric scattering towards this band (λ^{-4} molecular spectral dependence due to Rayleigh scattering and typical λ^{-1} dependence for aerosol particles/water droplets) [6].

The emission sub-system is based on a 20-Hz repetition-rate, Q-switched, Nd:YAG solid-state pulsed laser providing light emission at 1064, 532 and 355-nm wavelengths by means of second- and third-harmonic generators (SHG and THG, respectively) from a fundamental wavelength of 1064 nm. 355 nm is, however, the wavelength of interest for characterisation of the optical atmospheric parameters. The reception sub-system, which is coaxially arranged with the emission optical axis (see Fig. 3), is based on a 1.8-m diameter, 1.8-m focal-length parabolic mirror (adapted from a Cassegrainian telescope) for collecting the returned light signal. In its focus a liquid light guide is used to convey the composite atmospheric return radiation (elastic plus Raman) from the telescope focal plane to the polychromator unit (i.e., the spectrally selective unit in reception). The guide collection efficiency is, approximately, $\xi_{PSF} = 90\%$ (this figure being computed from the light spot overspill on the guide aperture due to the point-spread function (PSF) of the telescope).

The polychromator (Tab. 2 and Fig. 3b) is formed by a condenser lenses (L1-L2 in Fig. 3b), a dichroic mirror (M1), interference filter (IF1), and focusing lenses (L3-L4). The condenser lens (L1) nearly collimates the composite light beam emerging from the liquid guide at the polychromator input (at this point note that perfect collimation is not possible because the guide end is an extended light source). The dichroic mirror (M1) separates the composite light return into two optical paths, one for the 355-nm wavelength (elastic-channel) and another for the 387-nm wavelength (Raman-channel), at the end of

which pertinent PMT (Photo-Multiplier Tubes)-based detectors are located (D1 and D2, respectively). Lenses (L2-L4) are used to focus light on the active area of the detectors. A ZEMAX™ ray-tracing computed-aided design (CAD) software has been used to ensure that the reception field of view is the same for both channels.

Signal acquisition is carried out by means of Licel™ transient recorders, which combine a 20 Msps, 12-bit, analog-to-digital converter (ADC) with a 250-MHz count-rate, 50-ns bin time, photon counter architecture, thus, enabling simultaneous analog and photon-counting acquisition modes in each lidar channel. The elastic channel is acquired in analog mode, which is the usual one when dealing with high light level signals (see Sect. 3.2), while the Raman channel is acquired in mixed analog/photon-counting mode. In the near-range of the Raman channel, where the return signal is more intense, the analog mode is used; in the far-range, where the signal is much weaker, the photon-counting mode is used [9]. The opto-electronic receivers can be controlled thanks to a specific CPU-distributed design by means of a user-friendly LabView™ interface.

3. SYSTEM LINK BUDGET: PERFORMANCE AND DISCUSSION

3.1. Opto-atmospheric parameter modelling

In order to assess system performance (estimated power levels, SNR, and estimated maximum system range for both the elastic and Raman channels), oversimplified opto-atmospheric profiles are preferred to complex realistic ones. The two-component atmospheric model presented next simulates an aerosol component consisting of a homogeneous load of aerosols up to the end of the boundary layer superimposed to a molecular component based on the US-standard atmosphere model [4].

3.1.1 Aerosol component

A wavelength-dependent aerosol component is modelled as a homogenous load of aerosols up to 3 km in height (atmospheric boundary layer (ABL)), which motivates the step-ladder profile of Fig. 4. Beyond the ABL a purely molecular atmosphere is considered.

A “clear air” atmospheric condition corresponding to a mean visibility margin (defined at a 532-nm reference wavelength), $V_M = 39.12\,km$, is simulated. According to Koshmieder’s relationship [5], this visibility translates into an aerosol extinction component, $\alpha_{532}^{aer} = 3.912/(V_M[km]) = 0.1\,km^{-1}$. A λ^{-1} aerosol wavelength dependency [7] is used to convert the aerosol extinction computed at the 532-nm wavelength (visible band, VIS) down to the desired 355-nm (elastic) and 387-nm (Raman) wavelengths in the UV.

Because, in contrast to the molecular component, there is not a theoretical aerosol extinction-to-backscatter ratio, a typical ratio of $S_{355}^{aer} = 25\,sr$ has been used by

interpolation of the visibility look-up table of [6], p.88. In general, the aerosol extinction-to-backscatter ratio (the so-called "lidar ratio") is a major environmental parameter depending on the climatology and seasonal variability of the site and operational wavelength.

3.1.2 Molecular component

The atmospheric molecular component due to Rayleigh scattering is based on the well-known US-standard atmosphere model [4] in which "standard air" is defined as dry air at 1013.25 hPa, 15 ºC (288.15 K), and 360 ppm volume concentration of CO_2. The US-standard atmosphere model uses predetermined pressure and temperature gradients and user-input ground-level temperature/pressure boundary conditions to compute the dry-air molecular number density, $N_{DryAir}(R)$, and the height-dependent refractive index, from which the molecular scattering cross section is derived. In the simulation, "standard-air" ground pressure and temperature conditions have been used. The wavelength dependency of the scattering cross section (and, therefore, of the molecular extinction and backscatter parameters) is assimilated by a λ^{-4} term according to classic Rayleigh's resonator theory and inclusion of the King's factor (also known as F-factor) for fine modelling of the wavelength dependency. The molecular extinction-to-backscatter ratio is the well known $8\pi/3$ Rayleigh's ratio.

Because Raman scattering is just molecular scattering in which the reception wavelength is red-shifted from the incident wavelength, the Raman backscatter profile is based on the same molecular model. Thus, the N_2-Raman backscatter $\left[m^{-1}sr^{-1}\right]$ at the return wavelength λ_R is computed as

$$\beta_{\lambda_R}(R) = N_{N_2}(R)\frac{d\sigma_{\lambda_R}(\pi)}{d\Omega}, \tag{1}$$

where $N_{N_2}(R)$ is the range-dependent nitrogen molecule number density [molecules/m^3] and $d\sigma_{\lambda_R}(\pi)/d\Omega$ is the range-independent differential Raman backscatter cross section at λ_R per solid angle unit [23.15×10^{-35} m^2/(molecule·sr) at 387 nm] [3]. Recalling that N_2 forms a constant fraction (≈78.084%) of dry air in the lower atmosphere, it follows that $N_{N_2}(R) \approx 0.78084 N_{DryAir}(R)$. Fig. 4 plots the molecular and aerosol extinction components as a function of height.

3.2. Assessment of system performance

3.2.1 Return Power Levels

Elastic channel.- Following [6][14], the elastic lidar equation (single-scattering, no-absorption assumption) is defined as

$$P_{\lambda_0}(R) = \frac{K}{R^2}\left[\beta_{\lambda_0}^{aer}(R) + \beta_{\lambda_0}^{mol}(R)\right]\exp\left\{-2\int_0^R\left[\alpha_{\lambda_0}^{aer}(r) + \alpha_{\lambda_0}^{mol}(r)\right]dr\right\}\xi_{\lambda_0}(R), \quad (2)$$

where $P(R)$ is the range-dependent power [W], $\beta(R)$ is the atmospheric volume backscatter coefficient [$m^{-1}sr^{-1}$], $\alpha(R)$ is the range-dependent extinction coefficient [m^{-1}], super-indexes "aer" and "mol" stand respectively for "aerosol" and "molecular" components, λ_0 is elastic-channel wavelength, R is the range [m], and K [Wm^3] is the system constant expressed as

$$K = \frac{Ec}{2}A_r, \quad (3)$$

where E is the transmitted energy [J], c is the light-speed [m/s], and A_r is the telescope effective receiving area [m^2]. $\xi_{\lambda_0}(R)$ in Eq.(2) is the geometrical overlap function expressing the range-dependent cross-over factor between the emitted laser beam and the telescope field of view and is unity due to coaxial laser-telescope arrangement.

In Eq.(2) the exponential term represents the two-way path total atmospheric transmittance due to molecules and aerosols,

$$T(\lambda_0, R)^2 = \exp\left\{-2\int_0^R\left[\alpha_{\lambda_0}^{mol}(r) + \alpha_{\lambda_0}^{aer}(r)\right]dr\right\}. \quad (4)$$

For a vertically-pointing lidar system, as is the case, R can be assimilated to the vertical coordinate, z, however, R is retained here for completeness in the definition of the lidar equation.

Raman channel.- In comparison with the elastic-backscatter lidar equation, in which both the optical emission path (i.e., from the laser source to the atmosphere) and return path (i.e., from the atmosphere back to the telescope) were operating at the same wavelength, λ_0, in the Raman case, the emission path operates at λ_0 while the return path operates at the Raman-shifted wavelength, λ_R. This translates into the two-way path Raman transmittance [14][3],

$$T(\lambda_0, R)T_R(\lambda_R, R); \quad T(\lambda_i, R) = \exp\left\{-\int_0^R\left[\alpha_{\lambda_i}^{mol}(r) + \alpha_{\lambda_i}^{aer}(r)\right]dr\right\} \quad (5)$$

with $\lambda_i = \lambda_0, \lambda_R$, instead of the two-way path elastic transmittance, $T(\lambda_0, R)^2$, of Eq. (4). Since the Raman receiver is specifically tuned to receive backscattered radiation from N_2 atmospheric molecules at the Raman-shifted wavelength, λ_R=387 nm, for an emission wavelength, λ_0 =355 nm, the Raman backscatter coefficient $\beta_{\lambda_R}(R)$ is computed from Eq. (1). Formally, the Raman lidar equation takes the form

$$P_{\lambda_R}(R) = \frac{K}{R^2}\beta_{\lambda_R}(R)\exp\left\{-\int_0^R\left[\alpha_{\lambda_0}^{mol}(r) + \alpha_{\lambda_0}^{aer}(r) + \alpha_{\lambda_R}^{mol}(r) + \alpha_{\lambda_R}^{aer}(r)\right]dr\right\}\xi_{\lambda_R}(R), \quad (6)$$

where atmospheric absorption effects have been neglected. As in Eq.(2), $\xi_{\lambda_R}(R)$ represents the geometrical overlap function at λ_R and is unity due to coaxial laser-telescope arrangement.

Fig. 5(a) simulates the range-corrected power return signals incident on the telescope at the elastic and Raman wavelengths according to Eq.(2) and Eq.(6), respectively. The simulation range is 200 m to 15 km. Because of the large dynamic range of the lidar signals spanning some 4 orders of magnitude in both channels, simultaneous analog and photon-counting recorded data will be glued according to the procedure described in [18][19]. Besides, a gated PMT solution (i.e., including an electronic enable/disable feature) will be used to disable reception during the first 200 m of the lidar signal where, due to the laser-telescope coaxial arrangement, the detectors become blinded. For the elastic channel, it is envisaged inclusion of neutral density filters to accommodate the return power levels of Fig. 5a to levels comparable to those of the Raman channel, since with such a large-aperture telescope, the input light levels can drive the PMT detector deep into saturation [from Fig. 5a and the PMT current responsivity, $R_i = 1.1\times10^5\ A/W$ in Tab 1, the photo-induced current at 6 km is 10 mA, a figure well above reported experimental maximum pulsed-current saturation ratings (1.6 mA for 0.1% detector linearity in the case of PMT 7400U [18])].

Channel transmissivity.- The channel transmissivity ($0 \le \xi \le 1$) is defined as the product of the individual subsystem transmission factors (i.e., the inverse of the optical losses) along the optical receiving chain. Formally,

$$\xi(\lambda) = \xi_T(\lambda)\xi_{PSF}(\lambda)\xi_g(\lambda)\xi_{poly}(\lambda), \tag{7}$$

where $\lambda = \lambda_0, \lambda_R$ is the elastic/Raman reception wavelength, $\xi_T(\lambda)$ is the telescope transmission, $\xi_g(\lambda)$ is the liquid-guide transmission, $\xi_{PSF}(\lambda)$ is the guide-to-telescope coupling efficiency due to the PSF of the telescope (Sect. 2), and $\xi_{poly}(\lambda)$ is the total polychromator transmission defined as

$$\xi_{poly}(\lambda) = \xi_{dichr}(\lambda)\xi_{lens}(\lambda)^n\xi_{IF}(\lambda), \tag{8}$$

where $\xi_{dichr}(\lambda)$, $\xi_{lens}(\lambda)$, and $\xi_{IF}(\lambda)$ are the dichroic mirror (D1), lenses (L1-L4), and interference-filter transmission factors, respectively, from Tab 2. In Eq.(8), $n = 3$ for all the lenses in each channel of the polychromator are assumed identical transmissivities.

The elastic/Raman channel transmissivities according to Eq.(7) are listed in Tab. 1 along with the channel voltage responsivity (or net voltage responsivity),

$$R_v'(\lambda) = R_i(\lambda)G_T\xi(\lambda), \tag{9}$$

defined as the product of the current responsivity of the detector, R_i [A/W], times the transimpedance gain G_T ($G_T = R_{in} = 50\Omega$, i.e., the input impedance of the transient recorder), times the channel transmissivity, $\xi(\lambda)$ from Eq.(7) above.

3.2.2 Signal-to-Noise Ratio

SNR formulation for the elastic and Raman channels depends upon the detection mode used in the acquisition unit (see Sect. 2). In what follows, the elastic channel is acquired in analog mode while the Raman channel is acquired in mixed analog/photon-counting mode (data is glued by software). In any case, the medium/far-range of the Raman signal is always acquired in photon-counting mode.

I. Analog-detection mode.- The SNR under analog-detection mode can be expressed as (adapted from [8])

$$SNR_a(R) = \frac{R_v' P(R)}{\sqrt{N_{sh,s}(R) + N_{sh,b} + N_{sh,d}}}, \tag{10}$$

where R_v' [V/W] is the net voltage responsivity (Eq.(9)), $P(R)$ [W] is the range-dependent return power at the telescope input (Eqs.(2),(6)), and N_x [V^2] is the noise variance. Subindexes $x = "sh,s","sh,b","sh,d"$ stand for "lidar signal-induced" shot noise, "background-induced" shot noise, and "dark" shot noise. For convenience, the noise variance, $N_x = \sigma_x^2 B_N$, is expressed as the product of the noise spectral density, $\sigma_x^2 \left[V^2/Hz\right]$ times the reception-channel noise-equivalent bandwidth, B_N [Hz]. The noise spectral densities are computed as

$$\sigma_{sh,s}^2(R) = 2qG_T^2 FM^2 R_{io} P(R) \xi \tag{11}$$

$$\sigma_{sh,b}^2 = 2qG_T^2 FM^2 R_{io} P_{back} \xi \tag{12}$$

$$\sigma_{sh,d}^2 = 2qG_T^2 \left(I_{ds} + FM^2 I_{db}\right) \tag{13}$$

$$\sigma_{th}^2 = \sigma_{th,i}^2 G_T^2 \tag{14}$$

where $P(R)$ and P_{back} are respectively the lidar- and background-received powers, q is the electron charge, G_T is the transimpedance gain (i.e., the acquisition unit input impedance, $G_T = R_{in} = 50\Omega$), F and M are, respectively, the detector excess-noise factor and multiplication gain, R_{io} is the detector intrinsic responsivity [A/W] ($R_{io} = R_i/M$ from the PMT manufacturer's specs in Tab. 1 with R_i the PMT anode-current responsivity [A/W]), ξ is the channel transmissivity (Eq.(7)), I_{ds} and I_{db} are, respectively, the surface and volume dark currents of the detector ($I_{ds} = 0$ for a PMT, $I_{db} = I_d/M$ from Tab. 1), and $\sigma_{th,i}^2$ is the thermal variance of the acquisition unit, $\sigma_{th,i}^2$ [V^2/Hz]. Without need of Eq.(14), σ_{th}^2 is directly, $\sigma_{th}^2 = 4kTR_{in}$, with k the Boltzmann's constant, $T = 300K$ the noise equivalent temperature, and $R_{in} = 50\Omega$ the input impedance of the transient recorder.

II. Photon-counting detection mode.- In photo-counting mode, pulse height fluctuations (photon pile-up) can be reduced by setting a discriminator level on the pulse height, therefore allowing a significant improvement on the SNR. Besides, thermal noise can be ignored by setting a PMT gain sufficiently high, so that the discriminator level source can be easily set higher than amplifier noise level [9]. In the following SNR model, the effect of the discriminator level on the SNR is neglected so that the model gives a conservative lower bound on the expected SNR.

The SNR expression under photon-counting detection takes the form [9]

$$SNR_{pc} = \frac{N_s' \sqrt{\tau}}{\sqrt{N_s' + 2(N_b' + N_d')}}, \tag{15}$$

where N_s' is the (mean) number of counts per second due to the lidar return signal, N_b' is the (mean) number of counts per second due to the background light, and N_d' is the (mean) number of count per second due to the PMT dark current. The factor 2 in the denominator accounts for the fact that N_s' is calculated by subtracting to the total number of counts per second $\left(N_s' + N_b' + N_d'\right)$, the background and dark component $\left(N_b' + N_d'\right)$, which results in double variance contribution from the $\left(N_b' + N_d'\right)$ term. In Eq.(15) it is easy matter to relate the mean number of counts per second to power concept in units of [W] as introduced in Sect. 3.2.1. For example, $N_s' = P_{\lambda_R}(R)\xi(\lambda_R)R_{io}/q$ (refer to Eqs.(6)-(7)).

Fig. 5(b) plots the assessed SNR versus range for both the elastic channel (Eq.(10), analog mode) and the Raman channel (Eq.(10), analog mode; Eq.(15), photon-counting mode). At this point, it is important to notice that SNRs have been computed under night-time operation (background radiance, $L=2.7\times10^{-13}$ $Wcm^{-2}nm^{-1}sr^{-1}$ [21] for this will the operational mode of the lidar.

Fig. 6 provides a more insightful analysis on the different noise variance components contributing to the system SNR (variances are computed in analog mode for the elastic channel and in photon-counting mode for the Raman channel for the latter is most significant mode of operation for the Raman channel in terms of noise performance). It is seen that both channels operate in signal-induced shot-dominant regime, which ensures a slow $\sqrt{P(R)}$ decay in the SNR (i.e., nearly proportional to a $1/R$ decay for clear atmospheres) in front of a faster $1/R^2$ decay, which is characteristic of all other noise-dominant regimes [7]. When comparing the background- with the dark-noise variance, the latter is always below or slightly below the background variance, which evidences quiet PMT detectors and a sufficient selection of the interference filter bandwidth (10 nm for both channels, Tab. 1).

III. Channel Noise Equivalent Power (NEP).- The channel NEP (also called "system NEP" $\left[W/\sqrt{Hz}\right]$) is defined in *analog detection mode* and departs from the well-know

concept of noise expressed in power units [W] (i.e., referred to the telescope input) [7][9] but assimilating both detector dark-noise and transient-recorder thermal-noise contributions in the receiving channel. Formally,

$$NEP_s = \frac{\left(\sigma_{sh,d}^2 + \sigma_{th}^2\right)^{1/2}}{R_v'} \quad \left[\frac{W}{\sqrt{Hz}}\right], \tag{16}$$

where $\sigma_{sh,d}^2$ and σ_{th}^2 (both in units of $\left[V^2/Hz\right]$) are, respectively, the detector dark-shot noise defined in Eqs.(13) and the acquisition-unit thermal-noise standard deviations $\sigma_{th}^2 = \sigma_{th,i}^2 G_T^2$ (being $\sigma_{th,i}^2$ the thermal variance of the acquisition unit). $R_v'\left[V/W\right]$ is the net voltage responsivity defined in Eq.(9). With the elastic- and Raman-channel specifications of Tab.1, the NEP_s figure obtained is 3.5 and 3.8 $fW/\sqrt{Hz}$, respectively, which corresponds to a detection sensitivity of about 1200 photons/s in analog mode.

In photon-counting detection mode, the thermal noise component can be ignored by setting a discriminator level higher than the thermal-noise level. In this mode, the detection limit is usually defined as the input light level corresponding to $SNR_{pc} = 1$. From Eq.(15), this limit can be approximated by $N_s' = \sqrt{2N_d'}$ [9] (assumption of negligible background noise, $N_b' << N_d'$) with an error of less than about 30%, which yields a detection sensitivity of some 130 photons/s for the Raman channel.

3.2.3 Observation Time versus Maximum System Range

A convenient way to assess system performance is to estimate the maximum lidar range (under some predefined SNR goal criterion, SNR_{goal}) at each channel wavelength as a function of the required observation time. The SNR goal criterion is not unique for it ultimately depends on the specific optical-parameter inversion algorithm chosen and on the data-product inversion uncertainties acceptable from the user's side. Following ref. [2], Figs. 7-8, a SNR_{goal} in the 1-10 range is reasonable. For example, it is shown that under relatively clear atmospheric conditions (total homogeneous extinction, $\alpha_{tot} = 0.1km^{-1}$) the criteria $SNR_{goal} = 1$ and $SNR_{goal} = 10$ yield, respectively, 8% and 0.2% errors in the inverted optical atmospheric extinction when using an exponential-fitting inversion method. For a very clear atmosphere ($\alpha_{tot} = 0.01km^{-1}$), $SNR_{goal} = 1$ and $SNR_{goal} = 10$ yield 70% and 2% errors, respectively. A conservative figure of $SNR_{goal} = 10$ is set in what follows as in previous studies from the authors [17].

The maximum system range expresses the range where the lidar return voltage signal is SNR_{goal}-times the noise voltage standard deviation at the receiver output, that is, $SNR_v\left(R_{\max}\right) = SNR_{goal}$ in Eq.(10) (analog detection), or equivalently, $SNR_{pc}\left(R_{\max}\right) = SNR_{goal}$ in Eq.(15) (photon-counting detection) given an user-defined

observation time. The observation time, t_{obs}, is introduced from the number of time-averaged lidar pulses (temporal integration).

Since the SNR expressions in Eqs.(10),(15) are defined on a "single-pulse" basis (i.e., in response to a single laser pulse emitted) accounting for temporal pulse integration implies a SNR improvement equal to the square root of the number of integrated pulses, n_i [20]. Therefore, the maximum range condition for an observation time t_{obs} corresponding to n_i integrated pulses is formulated as

$$SNR_X(R_{\max})\sqrt{n_i} = SNR_{goal}, \tag{17}$$

where subindexes $X = "a" \; and \; "pc"$ stand for "analog" detection (Eq.(10)) and "photon-counting" detection modes (Eq.(15)), respectively. Using that $n_i = PRF \cdot t_{obs}$ with PRF the pulse repetition frequency of the laser source,

$$SNR_X(R_{\max}) = \frac{SNR_{goal}}{\sqrt{PRF \cdot t_{obs}}}. \tag{18}$$

Eq.(18) is an implicit relationship that given an observation time, t_{obs} and Eqs.(10), (15) enables to solve the maximum range, $R_{\max}$ associated to that t_{obs}, so that a point $(t_{obs}, R_{\max})$ of the locus "observation time – maximum range" is obtained.

The assessed $R_{\max}$ vs. observation time for both system channels is plotted in Fig. 7 for the "clear" atmospheric condition defined in Sect. 3.2.3. The Raman-channel simulation shows that for a 0 m a.s.l. ground –based lidar an observation time of about 0.4 s is enough to surpass the boundary layer ($R_{\max} = R_{PBL} \approx 3km$) and that for 10-s observation time, the maximum range is $R_{\max} \approx 10km$, thus reaching the top of the troposphere. In the case of the elastic channel (which is comparatively 3 orders of magnitude more intense than the Raman channel, see Fig. 5a) even operating on a single pulse basis ($n_i = 1$) $R_{\max} \approx 10km$ is easily reached.

4. CONCLUSIONS

A 1+1 elastic/Raman channel configuration operating night-time at 355/387-nm wavelengths has been proposed as the co-operative atmospheric-attenuation calibration sensor for the Cherenkov Telescope Array (CTA) under construction. Concept design of the IFAE/UAB lidar system has been presented in terms of an engineering overview of the main subsystems involved (Sect. 2), system specs (Tab. 1) and estimated system performance (Sect. 3.2). A simplified atmospheric model along with an ad-hoc methodological link-budget formulation to estimate return-power signal levels, SNR, and maximum system range has been derived in Sect. 3. Major assessment data products of this study being Fig. 5-Fig. 7.

The lidar system is based on a 60-mJ energy, 20-Hz rep. rate, 355-nm tripled Nd:YAG source coaxially arranged with a 1.8-m aperture, 1.8-m focal-length parabolic mirror conveying light by means of a liquid-guide to a polychromator equipped with 22-mm diameter PMT detectors. The Raman channel exhibits return power levels some 3 orders of magnitude below the elastic channel and reaches the top of troposphere (10 km in height) with a $SNR_{goal} = 10$ (photon-counting detection) with just 10-s observation time (Fig. 7). Because of the large dynamic range of the lidar signal spanning some 4 orders of magnitude mixed Licel™ analog/photon-counting transient recorders are planned to be used along with a software data-gluing procedure.

Future work comprises construction of the lidar prototype, its co-location on the final CTA site, and development of an inversion toolbox for Cherenkov data calibration taking into account the opto-atmospheric parameters measured by the lidar. Neutral density filters are foreseen to be included in the elastic channel of the polychromator along with an electronic gating feature for the PMT detectors (both channels disabled below approx. 200 m) in order to avoid detector saturation.

All in all, the IFAE/UAB lidar holds promise of reducing the systematic uncertainties and increasing the observation duty cycle thanks to a better knowledge of the atmosphere.

5. ACKNOWLEDGEMENTS

The Universitat Politècnica de Catalunya (UPC) gratefully acknowledges the following entities for their contribution to the research activity on lidar remote sensing: European Union under the project ACTRIS (Aerosols, Clouds, and Trace gases Research Infrastructure Network) ref. nº FP7- INFRA-2010-1.1.16, the Spanish Ministry of Science and Innovation (MICINN) and FEDER (European Regional Development) under the project TEC2009-09106 and Complementary Actions CGL2009-08031-E/CLI ("Charmex") and CGL2008-01330-E/CLI. European Union for the European Erasmus Mundus Master on Research and Information Technologies (MERIT), lidar course on "Optical Remote Sensing I: Active" (coord. by Prof. F. Rocadenbosch). Generalitat de Catalunya/AGAUR (Agency for Management of University and Research Grants) is also thanked for Mr. D. Kumar's predoctoral fellowship. O. Blanch acknowledges the support from the Ramon y Cajal program of MICINN. M. Doro acknowledges the support of the CPAN Consolider-Ingenio 2010 of MICINN.

REFERENCES

[1] A. Behrendt, T. Nakamura, M. Onishi, R. Baumgart, and T. Tsuda, "Combined Raman lidar for the measurement of atmospheric temperature, water vapor, particle extinction coefficient, and particle backscatter coefficient," *App. Opt.,* **41**(36), 7657-7666 (2002).

[2] A. Ansmann, U. Wandinger, M. Riebesell, C. Weitkamp, and W. Michaelis, "Independent measurement of extinction and backscatter profiles in cirrus clouds by using a combined Raman elastic-backscatter lidar," *Appl. Opt.,* **31**(33), 7113-7131 (1992).

[3] H. Inaba, "Detection of Atoms and Molecules by Raman Scattering and Fluorescence," Chap.5 in *Laser Monitoring of the Atmosphere,* E.D. Hinkley, Ed., (Springer-Verlag, New York, 1976), pp.1543-206.

[4] B. A. Bodhaine, N. B. Wood, E. G. Dutton, and J. R. Slusser, ¨On Rayleigh Optical Depth Calculations,¨ *J. Atmos. and Ocean. Technol.,* **16**(11), 1854-1861 (1999).

[5] H. Koshmieder, "Theorie der Horizontalen Sichtweite," *Beitr. Phys. Freien Atmos.,* **12**, 33-53 (1924).

[6] R.T.H. Collis and P.B. Russell, "Lidar measurements of Particles and Gases by Elastic Backscattering and Differential Absorption," Chap.4 in *Laser Monitoring of the atmosphere,* E.D. Hinkley, Ed., (Springer-Verlag, New York, 1976), pp.71-102.

[7] R. M. Measures, "Interaction and Propagation of Radiation," Chap.4 in *Laser Remote Sensing: Fundamentals and Applications,* (Krieger, Malabar, Fla., 1992), pp. 138–145.

[8] F. Rocadenbosch, A. Comerón, and D. Pineda, "Assessment of lidar inversion errors for homogeneous atmospheres," *App. Opt.,* **37**(12), 2199-2206 (1998).

[9] "Photon Counting Using Photomultiplier Tubes," *Hamamatsu Photonics,* AN-TPHO9001E02 (Japan, May. 1998).

[10] F. Rocadenbosch, ¨Lidar-Aerosol Sensing, ¨ in *Encyclopedia of Optical Engineering,* D. D. Driggers, Ed., (Marcel Dekker, New York, 2003), pp. 1090-1102. ISSN 0.8247-0939-X (print format), ISSN 0-8247-0940-3 (electronic format).

[11] F. Rocadenbosch, ¨Lidar-Wind, Raman and Other Sensing, ¨ in *Encyclopedia of Optical Engineering,* Donald D. Driggers, Ed., (Marcel Dekker, New York, 2003), pp. 1114-1127. ISSN 0.8247-0939-X (print format), ISSN 0-8247-0940-3 (electronic format).

[12] R. Jenness, Jr., D.B. Lysak, Jr., and C. R. Philbrick, "Design of a lidar receiver with fiber-optic output," *App. Opt.,* **36**(18), 4278-4284 (1997).

[13] F. Rocadenbosch, I. Mattis, C. Böckmann, G. Pappalardo, J. Bösenberg, L. Alados-Arboledas, A. Amodeo, A. Ansmann, A. Apituley, D. Balis, A. Chaikovsky, A. Comerón, V. Freudenthaler, O. Gustafsson, G. Hansen, R. Mamouri, V. Mitev, C. Muñoz, D. Nicolae, A. Papayannis, C. Pérez, M. R. Perrone, A. Pietruczuk, M. Pujadas, J. P. Putaud, F. Ravetta, V. Rizi, M. Sicard, V. Simeonov, N. Spinelli, D. Stoyanov, T. Trickl, U. Wandinger, and M. Wiegner, "The European Aerosol Research Lidar Network (EARLINET): An Overview," in *Proc. IEEE International Geoscience and Remote Sensing Symposium (IGARSS),* Boston, MA, USA, 6-11 July 2008, vol. 2, pp. II-410 – II-413 (2008).

[14] F. Rocadenbosch, "Optical Remote Sensing I: Active", *Lecture notes,* European Master of Research on Information and Communication Technologies (MERIT), Universitat Politècnica de Catalunya (UPC), http://upcommons.upc.edu/ocw/gestor/index.php?id_assig=739-1054-58066&idtit=1054&idcentre=739&propia=yes. Accessed July 2011.

[15] M. Sicard, M. N. M. Reba, S. Tomás, A. Comerón, O. Batet, C. Muñoz, A. Rodríguez, F. Rocadenbosch, and J. J. Fuensalida, "Site-testing results by means of an aerosol backscatter lidar at the Roque de los Muchachos Observatory", *Monthly Notices of the Royal Astronomical Society,* **405,** 129-142, DOI: 10.1111/j.1365-2966.2010.16468.x (2010).

[16] WMO GAW (2007), Plan for the implementation of the GAW Aerosol Lidar Observation Network (GALION) (Hamburg, Germany, 27-29 March 2007) (WMO TD nº 1443).

[17] D. Kumar, M. Sicard, S. Tomás, C. Muñoz, F. Rocadenbosch, "Engineering of a water-vapour Raman elastic-backscatter lidar at the Politechnical University of Catalonia (Spain)," 13th International Symposium on Remote Sensing (Conference on Lidar Technologies, Techniques, and Measurements for Atmospheric Remote Sensing II), Stockholm (Sweden), Sept. 13-14, 2006. Proc. SPIE, Vol. 6367, Lidar Technologies, Techniques, and Measurements for Atmospheric Remote Sensing II (U. N. Singh, Ed.), pp. 63670U-1/63670U-12, (2006).

[18] Licel GmbH, "Analysis Example: Gluing Analog and Photon Counting Data", Sect. 9.4 in "Licel Ethernet Controller – Installation and Reference Manual", Oct. 14, (2007) and private communication from Bernd Mielke (Licel GmbH).

[19] D. P. Donovan, J. A. Whiteway, and A. I. Carswell, "Correction for nonlinear photon-counting effects in lidar systems," *Appl. Opt.* **32,** 6742-6753 (1993).

[20] R.J. Barlow, "Errors", Chap.4 in *Statistics: A Guide To The Use Of Statistical Methods In The Physical Sciences,* F. Mandl, R.J. Ellison, D.J. Sandiford, Eds., (Wiley, Chichester, England, 1989).

[21] R. Mirzoyan, "Cherenkov light observation with the HEGRA detector at the Roque de los Muchachos Observatory," *New Astronomy Reviews,* **42,** 547–551 (1998)."

[22] www.mpi-hd.mpg.de/hfm/HESS/, www.magic.mppmu.mpg.de, www.veritas.sao.arizona.edu/ (accessed July 2011).

[23] http://www.cta-observatory.org/ (accessed July 2011).

[24] P.C. Zimmer, J.T. McGraw, "Measurement Astrophysics (MAP) First Steps: LIDAR Measurements of Atmospheric Extinction", UNM Measurement Astrophysics Group, American Astronomical Society, AAS Meeting #215, #441.08; *Bulletin of the American Astronomical Society,* **42**, p. 401 (2010).

[25] A. De Angelis, "Very-high-energy gamma astrophysics," *Nuovo Cimento,* **C-32 N5-6,** 19 (2009).

[26] B. Rossi and K. Greisen, "Cosmic-Ray Theory," *Reviews of Modern Physics,* **13,** 240–309, (Oct. 1941).

[27] F.I. Boley, "Atmospheric Cherenkov Radiation from Cosmic-Ray Air Showers," *Reviews of Modern Physics,* **36,** 792–808, (July 1964).

[28] A. M. Hillas, "Cherenkov Images of EAS produced by primary gamma rays and by nuclei", Proc. of the 19th International Cosmic Ray Conference (ICRC), La Jolla, USA, Vol. 3, 445 (1985).

[29] S. J. Nolan, G. Puhlhofer, and P. M. Chadwick (HESS Collaboration), "Active atmospheric calibration for H.E.S.S. applied to PKS 2155-304," Prepared for 30th International Cosmic Ray Conference (ICRC 2007), Mérida, Yucatán, México, 3-11 Jul 2007.

[30] D. Dorner, K. Nilsson, and T. Bretz, "A method to correct IACT data for atmospheric absorption due to the Saharan Air Layer," American Institute of Physics (AIP) Conf. Proc., Vol. 1085, 677, (2009).

[31] M. Doro, "CTA - A Project for a New Generation of Cherenkov Telescopes,"' *Nucl. Instrum. Meth.,* **A 630**, 285 (2011).

[32] W. Hoffman, and M. Martínez (CTA Consortium Collaboration), M., "Design Concepts for the Cherenkov Telescope Array," *ArXiv e-prints* (2010) [astro- ph.IM/1008.3703].

LIST OF FIGURES

LIST OF TABLES

FIGURES

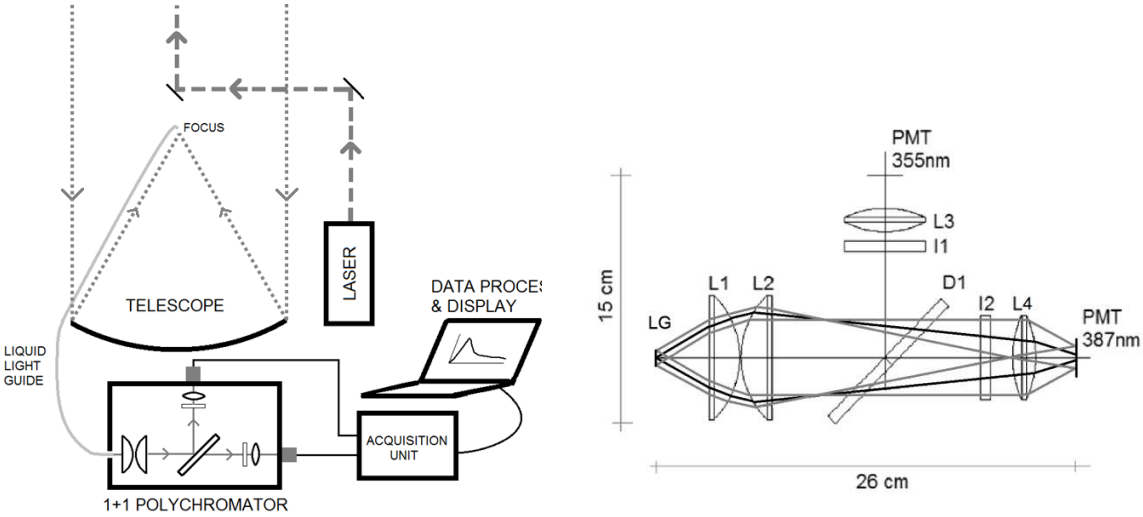

Fig. 3 Architecture of the IFAE/UAB 1+1 channel elastic/Raman lidar system. (a) Conceptual system arrangement. (b) Polychromator design layout and related ZEMAX™ ray tracing at 355 nm (elastic channel) and 387 nm (nitrogen Raman channel). (D1) Dichroic; (L1, L2, L3, L4) Lenses; (M1) Mirror; (I1, I2) Interference Filters.

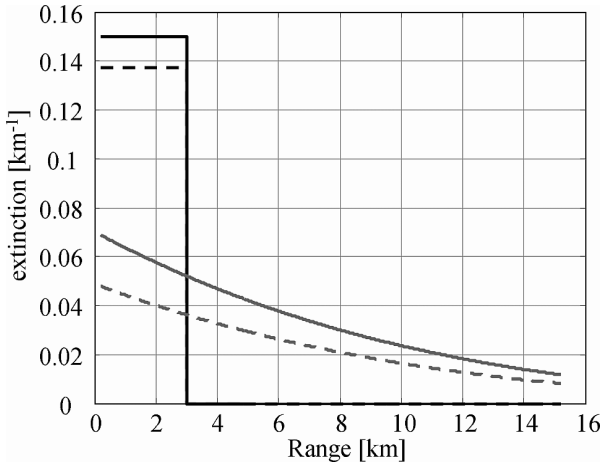

Fig. 4 Simulated opto-atmospheric parameters. (Step profiles) Aerosol (Mie) extinction profile. (Exponential-like profiles) Molecular (Rayleigh) extinction. In (solid trace) the elastic channels, in (dashed trace) the Raman ones.

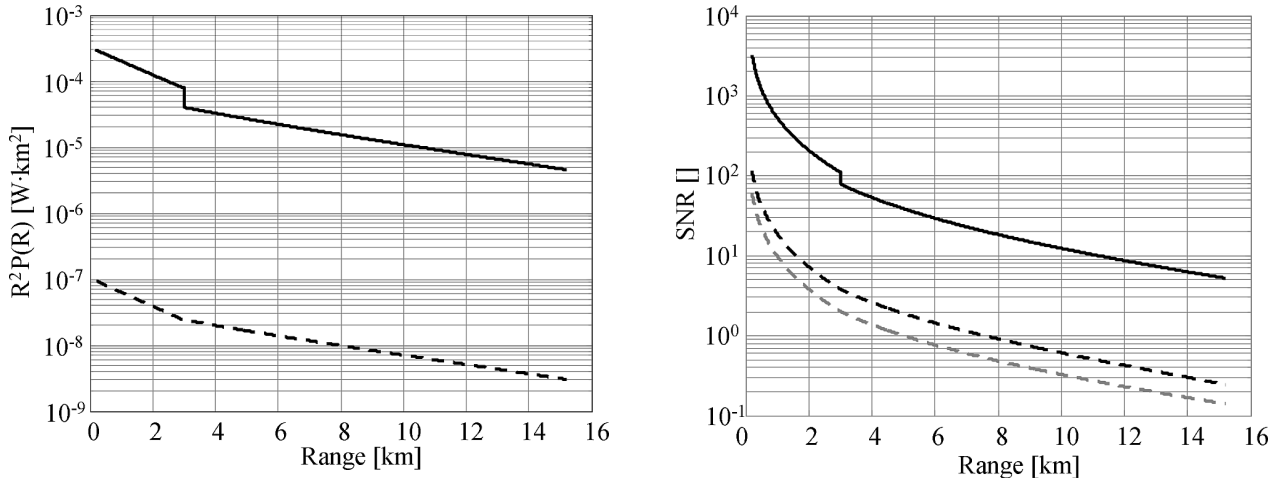

Fig. 5 Elastic/Raman channel performance under night-time operation. (a) Simulated range-corrected power levels. (b) Simulated signal-to-noise ratios (SNR). (Solid) Elastic channel. (Dashed black) Raman channel (photon-counting mode detection). (Dashed grey) Raman channel (analog mode detection). The step at 3 km in the elastic channel corresponds to the end of the atmospheric boundary layer.

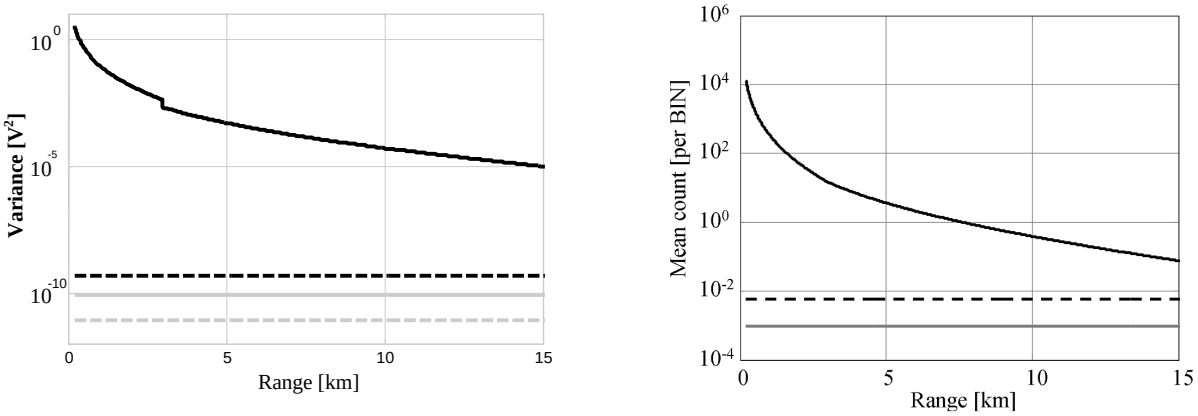

Fig. 6 Noise variances. (a) Elastic channel. (b) Raman channel. (Solid black) Signal-induced shot noise (Dashed black) Background-induced shot noise (night-time operation). (Solid grey) Dark shot noise.

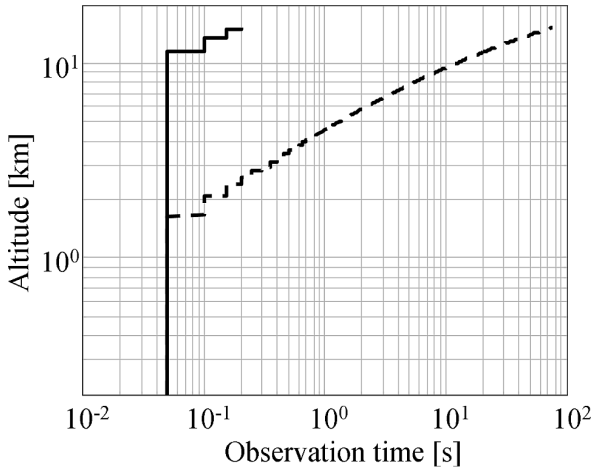

Fig. 7. Estimated maximum system range vs. observation time (night-time operation). Maximum system range condition, $SNR_{goal} = 10$. (Solid) Elastic channel. (Dashed) Raman channel.

TABLES

EMITTER		
Laser	Type Model Emitted wavelength, λ Energy per pulse, E Pulse Repetition Frequency, PRF Beam waist (diameter) Beam divergence, θ Pulse duration, τ_p	Nd:YAG Quantel Brilliant 355 nm 60 mJ 20 Hz 6 mm 0.5 mrad 5 ns
RECEIVER		
Telescope	Geometry Diameter, d Shadow diameter, d_{sh} Focal length, f Transmissivity, ξ_T	Cassegrain 1.8 m 0.08 m 1.8 m 0.55
	Liquid-guide-to-telescope coupling efficiency, ξ_{PSF}	0.9
Liquid Guide	Manufacturer & Model Active area diameter, d_b Numerical Aperture, NA Transmissivity, ξ_g	Lumatec Series 300 8 mm 0.59 (34º half-angle) >0.7 (in the UV)
Polychromator	*Ad hoc* design, see Tab. 2	
Photodetectors	Type PMT model Active area diameter, d_d	PMT Hamamatsu R1924A 22 mm
Acquisition unit (transient recorder)	Type Model	Mixed analog-to-digital converter (ADC) / Photon counter (PC) ADC 20 Msps 12bit / 250-MHz PC LICEL TR20-160

CHANNEL SPECIFICATIONS		
Wavelength	355 nm	387 nm (N_2)
Type	Elastic	Raman
Spatial Resolution	Up to 15 m in analog mode (10-MHz bandwidth), up to 7.5 m in photon-counting mode (50-ns bin)	
Polychrom. TX, ξ_{poly} (Eq.(8))	$0.90\times0.90^3\times0.60 = 0.39$	$0.90\times0.90^3\times0.65 = 0.43$
Channel transmissivity, ξ (Eq.(7))	0.15	0.16
Spectral Bandwidth, $\Delta\lambda$ [nm]	10	10
Type of Detector	PMT	PMT
Model	R1924A (Hamamatsu)	R1924A (Hamamatsu)
Internal Gain, M	2×10^6	2×10^6
Noise Factor, F	1.8	1.8
Dark current, I_d [nA]	3	3
Current responsivity, R_i [A/W]	1.1×10^5	1.1×10^5
Transimpedance gain (input impedance of the transient recorder) [Ω]	50	50
Channel responsivity, R_v' [V/W]	8.0×10^5	8.7×10^5
Channel NEP, NEP_s [fW/Hz$^{-1/2}$]	3.8	3.5

Tab. 1. 1+1 channel elastic/Raman lidar system specs.

Dichroic mirror Size *ρ, τ	1.5" DIA x 0.25"T ρ ≥ 90% @ 355nm τ ≥ 90% @ 387 nm

Lenses	Diameter (mm)	Effective Focal Length (mm)	Model (THORLABS)
Plano Convex Lens (L1 & L2)	75	38.0	LA1238
Bi convex Lens (L3 & L4)	50.8	60	LB1723

Interference Filters (I1 & I2)		
CWL (nm.)	355 ± 1.5	387 ± 1.5
FWHM (nm.)	10 ± 2.0	10 ± 2.0
% τ	Peak > 60%	Peak > 65%

Tab. 2 Polychromator specs of the 1+1-channel elastic/Raman polychromator. ρ and τ respectively represent reflectivity and transmissivity. Also, DIA and T respectively stand for diameter and thickness. All lenses transmission is 90%.